Microstructure in plasticity without nonconvexity

Amit Das[1], Amit Acharya[2], Pierre Suquet[3]

[1]Indian Institute of Technology, Bombay, India
[2]Carnegie Mellon university, Pittsburgh, USA
[3]Laboratoire de Mecanique et d Acoustique, CNRS, Marseille, France

Abstract

A simplified one dimensional rate dependent model for the evolution of plastic distortion is obtained from a three dimensional mechanically rigorous model of mesoscale field dislocation mechanics. Computational solutions of variants of this minimal model are investigated to explore the ingredients necessary for the development of microstructure. In contrast to prevalent notions, it is shown that microstructure can be obtained even in the absence of non-monotone equations of state. In this model, incorporation of wave propagative dislocation transport is vital for the modeling of spatial patterning. One variant gives an impression of producing stochastic behavior, despite being a completely deterministic model. The computations focus primarily on demanding macroscopic limit situations, where a convergence study reveals that the model-variant including non-monotone equations of state cannot serve as effective equations in the macroscopic limit; the variant without non-monotone ingredients, in all likelihood, can.

(To appear in Computational Mechanics)

Introduction

A long-standing goal of modern plasticity theory at the meso/macro scale is to model physically observed microstructure. In this paper, we define microstructure as spatial inhomogeneity in the plastic strain distribution and its development as the question of instability of a spatially uniform plastic strain distribution to small perturbations. In more common language this issue is also termed as the spontaneous emergence of patterns, and the models we develop and deal with here belong to the class of pattern-forming equations.

The minimum ingredients necessary to predict microstructure in plasticity are believed to be non-monotone equations of state arising from non-convex (incremental) energy (Aifantis, 1984; Ortiz and Repetto, 1999), or reaction diffusion equations with Cahn-Hilliard (CH) or Ginzburg-Landau (GL) structure (Walgraef and Aifantis, 1985,I, II, III; Glazov, Llanes and Laird 1995). In this paper, we show that the simplest models derived from Phenomenological Mesoscale Field Dislocation Mechanics, i.e. PMFDM (Acharya and Roy, 2006; Acharya, 2010, building on work from the same group from 2001 onwards) produces spatial patterning with similarities to 'cell-wall' fatigue microstructures without any non-monotone equations of state but due to wave-propagative dislocation transport. An important motivation for our study is that (P)MFDM in its full-blown multi-dimensional system form, as well as very closely related, if not identical, models have been shown to produce the emergence of microstructural features without any non-convexity in extensive numerical computations (Roy and Acharya, 2006; Limkumnerd and Sethna, 2006; Chen et al., 2010; Choi et al., 2012; Chen et al. 2013). Another recent work with many mathematically similar features as PMFDM but more complicated constitutive structure related to multiple-slip behavior (Xia and El-Azab, 2015) shows the development of realistic microstructure related to plastic response. It is our intention here to try to understand this phenomenon in PMFDM in as simple a setting as possible.

We also demonstrate stick-slip behavior arising from a non-convex energetic constitutive statement for kinematic hardening, admittedly of undecidable physical origin. Combinations of dislocation transport with the resulting non-monotone back stress produce very rich behavior consisting of apparently random nucleation of fronts of plastic deformation and their motion under spatially uniform applied stress.

1. Model

1.1. *Physical description*

We adapt an ansatz producing an exact time-dependent, quasi-static, 1-dimensional problem of Field Dislocation Mechanics from Acharya (2010). Symbols with a subscript x represent a spatial partial derivative while a subscript t represents a temporal partial derivative. Consider a long cylinder of rectangular cross-section as shown in Fig. 1. The cylinder is subjected to simple shear by applying spatially uniform shear traction $T(t)$ on the top surface while holding the bottom surface fixed. It is assumed that at any time t all stress and distortion fields vary only along the axis of the cylinder. Consistent with the

applied loading, it is assumed that the yz component of the total displacement gradient is the only non-zero one and it is homogeneous on the body. The only non-zero components of stress field are the shear stress $T(t)$ in the y direction on planes with normal in the z direction and its associated symmetry-related component. Likewise, the only non-zero component of plastic distortion is φ which represents plastic shearing in the y direction on planes with normal in the z direction. The spatial gradient of plastic distortion φ_x represents the only component of the (polar) dislocation density field representing screw dislocations with line and Burgers vector along the y direction. In this work we model plasticity at the mesoscale and consequently think of plastic strain rate produced by motion of the dislocation density field plus that due to the motion of unresolved 'statistical' dislocations, the latter modeled by more-or-less conventional constitutive assumptions from macroscopic plasticity theory.
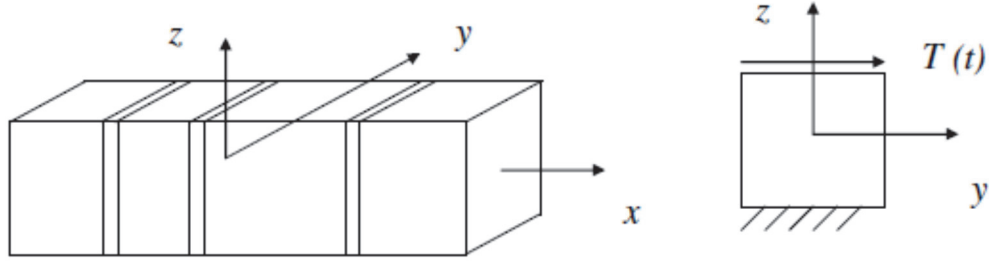

Fig. 1 Cylinder subjected to simple shear

The governing equation for the evolution of plastic distortion φ is derived here based on Acharya (2010). The dissipation, D, in this 1-d setting may be written as

$$D := \int_B 2T\left\{\frac{1}{2}\left(\varphi+\varphi^e\right)_t\right\}dv - \int_B \psi_t dv, \tag{1}$$

where T and φ^e are the yz component of the stress and elastic distortion respectively, and $\varphi+\varphi^e$ is the same component of the total displacement gradient tensor. The free energy density, ψ, is supposed to be of the form

$$\psi = \hat{\psi}\left(\varphi^e\right) + \frac{\varepsilon}{2}\varphi_x^2 + G(\varphi). \tag{2}$$

Here, $\varepsilon = O\left(\mu b^2\right)$ is a small parameter of the order of the shear modulus (μ) times the Burgers vector magnitude (b) squared.

The first term of (2), models the energy stored in the body due to elastic deformation. The second models the energy stored in dislocation cores, while the third term is associated

3

with the phenomenological energy content of unresolved statistical density that produces kinematic hardening. Stress can be obtained from free energy density as follows:

$$T = \frac{\partial \psi}{\partial \varphi^e}. \tag{3}$$

Substituting (2) and (3) in (1) we get

$$D = \int_B T\varphi_t dv - \int_B \varepsilon \varphi_x (\varphi_x)_t \, dv - \int_B \frac{\partial G}{\partial \varphi} \varphi_t dv. \tag{4}$$

Using the governing equations of the mesoscale field dislocation mechanics model (Acharya 2010; Acharya and Roy, 2006),it can be shown that in this simplified case the conservation law for Burgers vector content can be written as (see Appendix 1)

$$(\varphi_x)_t = -(\varphi_x V - L^p)_x$$
$$\Rightarrow \varphi_t = -\varphi_x V + L^p, \tag{5}$$

where the source term, L^p, arises in the governing equation as result of averaging (Acharya and Roy, 2006), and represents the plastic strain rate produced by 'unresolved' statistical dislocation density. Substituting (5) in (4),

$$D = \int_B \left(T - \frac{\partial G}{\partial \varphi}\right)(-\varphi_x V + L^p) dv - \int_B \varepsilon \varphi_x (-\varphi_x V + L^p)_x dv, \tag{6}$$

which implies

$$D = \int_B \left(T - \frac{\partial G}{\partial \varphi}\right)(-\varphi_x V + L^p) dv + \int_B \varepsilon \varphi_{xx} (-\varphi_x V + L^p) dv, \tag{7}$$

(where we have ignored a boundary term). Hence, the driving force for dislocation velocity, V, can be expressed as

$$V \rightarrow -\varphi_x \left(T - \frac{\partial G}{\partial \varphi} + \varepsilon \varphi_{xx}\right), \tag{8}$$

and that for L^p as

$$L^p \rightarrow \left(T - \frac{\partial G}{\partial \varphi}\right). \tag{9}$$

In (9), we retain the classical form of L^p, where the driving force is dependent only on stress and back-stress, and ignore the contributions of core energy. This enables a direct comparison with the conventional plasticity model. Nevertheless, we have tested the dissipation (7) while using (12) and found that it remains nonnegative throughout the entire simulation for various model set-ups as described in Section 2.

Assuming a simple 'linear' kinetic relation for V based on (8):

$$V = \frac{1}{\tilde{B}}\left[-\varphi_x \left(T - \frac{\partial G}{\partial \varphi} + \varepsilon \varphi_{xx}\right)\right], \tag{10}$$

4

where the drag coefficient $\tilde{B}$ is proportional to the magnitude of the polar density $|\varphi_x|$, the following expression for the evolution of plastic distortion tensor, φ, is obtained from (5) :

$$\varphi_t = \frac{|\varphi_x|}{B}\left[T - \frac{\partial G}{\partial \varphi} + \varepsilon \varphi_{xx} \right] + L^P .$$ (11)

The material constant B has physical dimensions of $stress \times time / length$. Equation (11) is an averaged equation modeling plastic behavior at the meso-scale. We assume L^p to be of 'standard' form

$$L^P = \dot{\gamma}_0 \left(\frac{\left| T - \frac{\partial G}{\partial \varphi} \right|}{g} \right)^{\frac{1}{m}} \mathrm{sgn}\left(T - \frac{\partial G}{\partial \varphi} \right)$$

$$g_t = |L^p|\left[k_0 |\varphi_x| + \theta_0 \left(\frac{g_s - g}{g_s - \tau_y} \right) \right],$$ (12)

following conventional plasticity assumptions of models with a back stress and power-law kinetics. Here, $\dot{\gamma}_0$ is a reference strain rate and g is the strength of the material which evolves according to a gradient modified standard Voce-law (Acharya and Beaudoin, 2000). The saturation stress is g_s, τ_y is the yield stress, and θ_0 is the Stage II hardening rate, k_0 is a parameter characterizing the hardening rate produced by the presence of polar density (containing a length scale), and m is the rate sensitivity.

An important goal for us in this paper is to understand what the addition of dislocation transport does to the conventional plasticity model in as simple a setting as possible. Thus, we would like to preserve the structure of (12). To simultaneously achieve this goal and ensure non-negative dissipation with our constitutive choices for V and L^p would require that the specific free energy cannot be defined as a function on the current state but rather as a functional on histories through the following rate equation (cf. Rice, 1971, Sec. 2.4):

$$\psi_t = \frac{\partial \hat{\psi}}{\partial \varphi^e} \varphi_t^e + \varphi_x \left(-\frac{\partial G}{\partial \varphi} + \varepsilon \varphi_{xx} \right) V\left(\varphi^e, \varphi, \varphi_x, \varphi_{xx}, g \right)$$

$$+ \left(\frac{\partial G}{\partial \varphi} \right) L^p \left(\varphi^e, \varphi, \varphi_x, \varphi_{xx}, g \right).$$ (13)

We utilize a non-monotoneback-stress term, $\partial G / \partial \varphi$, in the governing equation whose form is sinusoidal with amplitude proportional to the wavelength. It is assumed to arise from a nonconvex energy contribution of the form

$$G(\varphi) = \eta \sin\left(\frac{\varphi}{\eta} \right) \tau_y, \quad \eta \ll 1$$ (14)

where η is a nondimensional parameter. Since η is small, the contribution of the $G(\varphi)$ term in the energy is negligible. Thus, in practical terms, if back stress effects are determined from measurements of energy storage due to plastic strain (the part of it that is determined from the observable dislocation density field), then whether such terms may or may not be present in material behavior would be hard to decide. However, the back stress, $\partial G / \partial \varphi$, arising from such a small energy contribution can of course be of significant magnitude. An ODE of the form,

$$\dot{\varphi} = -\frac{\partial G}{\partial \varphi}(\varphi) + f, \qquad (15)$$

where f is a forcing function, is known to produce stick-slip behavior (e.g., Abeyaratne, Chu and James, 1996). The particular form of the $\partial G / \partial \varphi$ term does not have an influence as long as it is a high-frequency bounded oscillatory function with the same amplitude τ_y. Any high-frequency, bounded oscillatory function in the plastic strain with the same amplitude τ_y is expected to produce similar stick-slip behavior in the high frequency limit.

In recent experiments of micron-scale plasticity, stick-slip behavior has been observed (Dimiduk et al., 2006) and it has often been argued that its origins are stochastic (Parthasarathy et al., 2007). We show here that such behavior can be obtained from purely deterministic considerations. However, the primary shortcoming of this model is that the physical origin of such a small amplitude augmentation of the energy is not clear at this point. Thankfully, such an augmentation of the theory is not essential for producing spatial microstructure as we show in this paper. In the following, we refer to such oscillatory kinematic hardening related energy and back stress by the term *'wiggly,'* using terminology introduced by Abeyaratne et al. (1996) in a different context.

1.2. *Non-dimensionalization of governing equations*

We seek to non-dimensionalize the set of governing equations (11) and (12). Consider length, stress and time as the primary dimensions of the governing equations. The scaling parameter utilized for length variables is the length of the domain L, the stress variables is the yield stress τ_y, and the time variable is the reciprocal strain rate $\dot{\gamma}_0^{-1}$. We define the following dimensionless variables using the scaling parameters:

$$\tilde{x} = \frac{x}{L}, \quad \tilde{t} = t\dot{\gamma}_0, \quad \tilde{T} = \frac{T}{\tau_y}, \quad \tilde{G} = \frac{G}{\tau_y}, \quad \tilde{L}^p = \frac{L^p}{\dot{\gamma}_0} \quad \tilde{g} = \frac{g}{\tau_y}. \qquad (16)$$

We have

$$\varphi_t = \frac{\partial \varphi}{\partial t} = \frac{\partial \varphi}{\partial \tilde{t}} \frac{\partial \tilde{t}}{\partial t} = \dot{\gamma}_0 \frac{\partial \varphi}{\partial \tilde{t}}. \qquad (17)$$

Likewise,

6

$$\varphi_x = \frac{1}{L}\varphi_{\tilde{x}},$$

$$\varphi_{xx} = \frac{1}{L^2}\varphi_{\tilde{x}\tilde{x}}.$$

(18)

Substituting (16), (17) and (18) in the governing equation (11) we obtain

$$\dot{\gamma}_0\varphi_{\tilde{t}} = \frac{|\varphi_{\tilde{x}}|}{BL}\left[\tau_y\tilde{T} - \tau_y\frac{\partial\tilde{G}}{\partial\varphi} + \frac{\varepsilon}{L^2}\varphi_{\tilde{x}\tilde{x}}\right] + \dot{\gamma}_0\tilde{L}^P.$$

(19)

We rearrange (19) to get a non-dimensional form as follows:

$$\varphi_{\tilde{t}} = \frac{|\varphi_{\tilde{x}}|}{B^*}\left[\tilde{T} - \frac{\partial\tilde{G}}{\partial\varphi} + \varepsilon^*\varphi_{\tilde{x}\tilde{x}}\right] + \tilde{L}^P,$$

(20)

where B^* and ε^* are new constants defined as

$$B^* = \frac{BL\dot{\gamma}_0}{\tau_y}, \quad \varepsilon^* = \frac{\varepsilon}{\tau_y L^2}.$$

(21)

An important order-of-magnitude to keep in mind is that

$$\varepsilon^* = \frac{\mu}{\tau_y}\left(\frac{b}{L}\right)^2$$

(22)

so that a small value of ε^* may be interpreted as working close to the macroscopic limit where the domain size is much larger than the interatomic distance.

The non-dimensional form of L^p is given by

$$\tilde{L}^P = \left(\frac{\left|\tilde{T} - \frac{\partial\tilde{G}}{\partial\varphi}\right|}{\tilde{g}}\right)^{\frac{1}{m}} \mathrm{sgn}\left(\tilde{T} - \frac{\partial\tilde{G}}{\partial\varphi}\right).$$

(23)

The non-dimensional form of the hardening rate equation is obtained from

$$\dot{\gamma}_0\tau_y\tilde{g}_{\tilde{t}} = \dot{\gamma}_0\left|\tilde{L}^P\right|\left[\frac{k_0}{L}|\varphi_{\tilde{x}}| + \theta_0\left(\frac{g_s - \tau_y\tilde{g}}{g_s - \tau_y}\right)\right]$$

(24)

and then rearranging the terms to obtain

$$\tilde{g}_{\tilde{t}} = \left|\tilde{L}^P\right|\left[k_0^*|\varphi_{\tilde{x}}| + \theta_0^*\left(\frac{g_s^* - \tilde{g}}{g_s^* - 1}\right)\right],$$

(25)

where k_0^* and g_s^*, and θ_0^* are new constants defined as follows:

$$k_0^* = \frac{k_0}{L\tau_y}, \ g_s^* = \frac{g_s}{\tau_y}, \ \theta_0^* = \frac{\theta_0}{\tau_y}.$$ (26)

For the sake of convenience we drop the tilde and asterisk subscripts in the non-dimensional governing equations.

1.3. *Notation*

The following notation is followed in the numerical scheme described below. Consider the discrete field variable $\varphi^k(x_h)$. The superscript k indicates the time level counter starting from $k=0$, with discrete instants of time marked by t^k. We refer to $\Delta t^k = t^k - t^{k-1}$. The distance from the origin of the domain is indicated by the symbol x_h inside the brackets $(\ )$ which is the position of the hth node. The spatial and temporal derivatives are denoted by subscripts. The discrete spatial derivative of φ at time level k and location x_h is denoted by $\varphi_x^k(x_h)$. Likewise, the temporal derivative of φ at time level k and location x_h is denoted by $\varphi_t^k(x_h)$. The discrete double spatial derivative is denoted by $\varphi_{xx}^k(x_h)$. The notations $\frac{\partial G^k}{\partial \varphi}(\varphi^k(x_h))$ and $\frac{\partial^2 G^k}{\partial \varphi^2}(\varphi^k(x_h))$ represent partial derivatives of the function G with respect to φ, evaluated at time level k at the spatial location. $L^{p^k}(x_h)$ and $g^k(x_h)$ represent the value of L^p and g at time level k and location x_h.

1.4. *Numerical Scheme*

We follow Acharya *et al.* (2004) in formulating the scheme utilized to deal with wave like response. This scheme has been subsequently utilized in Das et al. (2012) and Zhang et al. (2015) for an extensive class of more complex problems in 1 and 2 space dimensions and time including nontrivial coupling with quasi-static and dynamic material deformation, some of which serve as verification and validation exercises for it, both individually and embedded in more complicated coupled algorithms. We have subsequently realized that the scheme is strongly related to a special and simple case of the robust methodology of Kurganov et al. (2001) for hyperbolic conservation laws and Hamilton-Jacobi equations.

The essential idea of the scheme is to identify the first order wave-like, second-order diffusion-like and (ordinary differential equation) source-like responses in the problem from the linearization of the pde for φ at each time level. Then at each spatial grid point an upwind direction is identified based on this exercise. In addition, time step constraints for wave, diffusion, and simple source behavior are evaluated at each spatial grid point based on standard stability considerations for consistent standard finite difference

8

approximations for constant coefficient, linear equations describing such behaviors. Finally, the minimum time-step arising from these evaluations is adopted in the scheme.

The linearization of non-dimensionalized form (20), ignoring the source term, is performed formally by taking its first variation :

$$\delta\varphi_t^k\left(x_h\right)=-\left(\frac{-\operatorname{sgn}\left(\varphi_x^k\left(x_h\right)\right)}{B}\right)\left[T^k-\frac{\partial G^k}{\partial\varphi}\left(\varphi^k\left(x_h\right)\right)+\varepsilon\varphi_{xx}^k\left(x_h\right)\right]\delta\varphi_x^k\left(x_h\right)$$
$$+\frac{\left|\varphi_x^k\left(x\right)\right|}{B}\left[-\frac{\partial^2 G^k}{\partial\varphi^2}\left(\varphi^k\left(x_h\right)\right)\right]\delta\varphi^k\left(x_h\right) \qquad (27)$$
$$+\frac{\left|\varphi_x^k\left(x_h\right)\right|}{B}\left[\varepsilon\delta\varphi_{xx}^k\left(x_h\right)\right].$$

The first term of (27) provides linearized wave-like behavior. A corresponding velocity $c^k\left(x_h\right)$ is obtained as follows

$$\delta\varphi_t^k\left(x_h\right)=-c^k\left(x_h\right)\delta\varphi_x^k\left(x_h\right)$$
$$+\frac{\left|\varphi_x^k\left(x_h\right)\right|}{B}\left[-\frac{\partial^2 G^k}{\partial\varphi^2}\left(\varphi^k\left(x_h\right)\right)\right]\delta\varphi^k\left(x_h\right)$$
$$+\frac{\left|\varphi_x^k\left(x_h\right)\right|}{B}\left[\varepsilon\delta\varphi_{xx}^k\left(x_h\right)\right], \qquad (28)$$
$$where\ c^k\left(x_h\right)=\left(\frac{-\operatorname{sgn}\left(\varphi_x^k\left(x_h\right)\right)}{B}\right)\left[T^k-\frac{\partial G^k}{\partial\varphi}\left(\varphi^k\left(x_h\right)\right)+\varepsilon\varphi_{xx}^k\left(x_h\right)\right].$$

To calculate $c^k\left(x_h\right)$ for a time level k and at a spatial location x_h the required values of $\varphi_x^k\left(x_h\right)$ and $\varphi_{xx}^k\left(x_h\right)$ are computed using central finite differences.

$$\varphi_x^k\left(x_h\right)\leftarrow\frac{\varphi^k(x_{h+1})-\varphi^k(x_{h-1})}{2d}$$
$$\varphi_{xx}^k\left(x_h\right)\leftarrow\frac{\varphi^k(x_{h+1})-2\varphi^k(x_h)+\varphi^k(x_{h-1})}{d^2}. \qquad (29)$$

Once $c^k\left(x_h\right)$ is obtained, depending on the sign of $c^k\left(x_h\right)$ the value of $\varphi_x^k\left(x_h\right)$ is updated in accordance with the upwind scheme as follows:

$$\varphi_x^k(x_h) := \frac{\varphi^k(x_{h+1}) - \varphi^k(x_h)}{d} \qquad if \quad c^k(x_h) < 0$$

$$\varphi_x^k(x_h) := \frac{\varphi^k(x_h) - \varphi^k(x_{h-1})}{d} \qquad if \quad c^k(x_h) > 0 \qquad (30)$$

$$\varphi_x^k(x_h) := \frac{\varphi^k(x_{h+1}) - \varphi^k(x_{h-1})}{2d} \qquad if \quad c^k(x_h) = 0 \cdot$$

where d is the element size.

The time step is computed as below, taking due account of the source term and linearized advection and diffusion:

$$\Delta t^k = \min_{all\ h} \left(\frac{d}{\left|c^k(x_h)\right|}, \frac{B}{\left|\varphi_x^k(x_h)\right|\left[-\frac{\partial^2 G}{\partial \varphi^2}\left(\varphi^k(x_h)\right)\right]}, \frac{d^2 B}{\varepsilon \left|\varphi_x^k(x_h)\right|}, \frac{0.002}{L^{p^k}(x_h)} \right) \cdot (31)$$

The following sequence of steps is followed to solve the governing equations(20) and (25) . The state at discrete time level k consists of nodal values of the discrete fields φ and g .

$$\frac{\varphi^{k+1}(x_h) - \varphi^k(x_h)}{\Delta t^k} = \frac{\left|\varphi_x^k(x_h)\right|}{B} \left[\begin{matrix} T^k - \frac{\partial G^k}{\partial \varphi}\left(\varphi^k(x_h)\right) + \\ \varepsilon \frac{\varphi^k(x_{h+1}) - 2\varphi^k(x_h) + \varphi^k(x_{h-1})}{d^2} \end{matrix} \right]$$
$$+ L^{p^k}(x_h) \quad if\ c^k(x_h) \neq 0 \qquad (32)$$

$$\varphi^{k+1}(x_h) = \frac{\varphi^k(x_{h+1}) + \varphi^k(x_{h-1})}{2} + L^{p^k}(x_h)\Delta t^k \quad if\ c^k(x_h) = 0.$$

$$\frac{g^{k+1}(x_h) - g^k(x_h)}{\Delta t^k} = \left(\frac{\left|T^k - \frac{\partial G^k}{\partial \varphi}\left(\varphi^k(x_h)\right)\right|}{g^k(x_h)} \right)^{\frac{1}{m}} \left[k_0\left|\varphi_x^k(x_h)\right| + \theta_0\left(\frac{g_s - g^k(x_h)}{g_s - 1}\right) \right] \cdot (33)$$

1.5. *Problem Set-up*

The list of parameters selected for performing the simulations is shown in Table 1.

Parameter	Description	Value
m	rate sensitivity	0.03
η	non-convex energy parameter	0.01
B^*	scaled drag coefficient	1
ε^*	scaled dislocation core energy parameter	$3.28\left(10^{-5}\right)$
$k_0^{\,*}$	scaled hardening parameter	400
$g_s^{\,*}$	scaled saturation stress	3.22
$\theta_0^{\,*}$	scaled stage II hardening parameter	7.84

Table 1: List of non-dimensional model parameters

Lengths are measured in units of L, time in units of $\dot{\gamma}_0^{-1}$, and stress in terms of τ_y.

The initial condition specified for φ is of the following form:

$$\text{Initial condition}: \varphi(x,0) = v\sin\left(\frac{N\pi x}{L}\right) \quad 0 < v \ll 1, \tag{34}$$

where the chosen value of v and N is equal to 0.001 and 500, respectively. This reflects a very small amplitude with high wave-number, N, perturbation to the zero plastic strain initial condition. Our goal in all cases is to probe the stability of a spatially homogeneous initial profile to this particular type of perturbation. Neumann boundary conditions of $\varphi_x = 0$ are applied at the ends of the domain. A linear ramp loading is specified for the simulations where the non-dimensional applied load parameter, $T(t)$, increases uniformly from zero to a finite value of stress, unless otherwise mentioned.

The initial condition for g is assumed to be 1 (non-dimensional).

Since the model is rate-dependent, it is expected that the rate of loading will have an influence in the response of the governing equation. The effect of different rates of loading on the behavior of the governing equation is not pursued in this section because our primary interest has been to show the development of spatial microstructure in the model.

Clearly, the initial condition we choose has large polar dislocation content even though it derives from a negligible plastic distortion profile. From the point of view of probing stability of evolution of plastic deformation, this is, of course, perfectly acceptable. In all cases involving dislocation transport, the dislocation density profile rapidly subsides to be non-detectable to visual inspection on evolution from the initial condition, much before initial yield and subsequent inhomogeneity development. However, the seeds of the

11

perturbation remain and without the perturbation in the initial condition no patterning develops. Thus we could as well have started with initial conditions as this slightly-evolved, almost-homogeneous plastic strain and dislocation density profile, if we knew their analytical form. Since we do not, we proceed as described in this paper.

In demonstrating our results, we often plot the spatial average of φ and its maximum value over the domain, denoted by φ_{avg} and φ_{max} respectively, as functions of time or applied load. φ_{avg} is computed as follows:

$$\varphi_{avg}^{k} = \frac{\sum_{h=1}^{P} \varphi^{k}(x_h)}{P}, \tag{35}$$

where P is the total number of nodes and φ_{avg} refers to φ_{avg}^{k} viewed as a function of k (or discrete time or load). φ_{max}^{k} represents the maximum value of φ, $\varphi_{max}^{k} = \max_{h} \varphi^{k}(x_h)$, over the entire set of spatial nodes at the kth time level, and a similar interpretation as before applies for φ_{max}. Step-like profiles in φ_{avg} beyond initial yield reflect stick-slip behavior on the average in the domain. (Near) discontinuous behavior in φ_{max} different from the φ_{avg} variation reflects spatially localized stick-slip behavior.

2. Results and discussion

2.1. *Case I: Model with dislocation transport, wiggly back stress, and gradient hardening*

The results of the simulations performed using the model described by ((20), (23),(25)), i.e.

$$\varphi_t = \frac{|\varphi_x|}{B}\left[T - \frac{\partial G}{\partial \varphi} + \varepsilon\ \varphi_{xx}\right] + L^P$$

$$L^P = \left(\frac{\left|T - \frac{\partial G}{\partial \varphi}\right|}{g}\right)^{\frac{1}{m}} \mathrm{sgn}\left(T - \frac{\partial G}{\partial \varphi}\right)$$

$$g_t = |L^p|\left[k_0\ |\varphi_x| + \theta_0\left(\frac{g_s - g}{g_s - 1}\right)\right]$$

are discussed in this section. Fig. 2 (a) is a plot of the evolution of φ for the simulation performed with the prescribed initial condition (34). A linear ramp loading where the non-dimensional applied load variable, $T(t)$, increases uniformly from 0 to 3.0 is specified. The value of η chosen for this simulation is equal to 0.01. From the initial condition, the profile quickly transforms into an almost homogeneous profile shown in Fig. 2 (a) (i). The corresponding φ_x profile has a uniform value close to 0 as shown in Fig. 2 (b) (i). A yield-

like behavior is observed, as expected from (23) where the φ profile remains almost unaltered until $T(t)$ reaches approximately a value of 2.0 before evolution occurs. This is due to the back–stress in the formulation – for $\varphi \approx 0$, $\partial_\varphi G \approx 1$ and the initial condition of $g = 1$ so that evolution occurs only when $T \approx 2$ for m small. This phenomenon is indicated in Fig. 2 (c) where the variation of average and maximum plastic distortion is plotted versus time. When the value of $T(t)$ increases beyond 2.0 the profile begins to rise and small kinks begin to develop in the profile as shown in Fig. 2 (a) (ii). These small kinks begin to grow as shown in Fig. 2 (a) (iii) and (iv) as the applied load increases, and develop into peaks representing inhomogeneous development in the φ profile. All the peaks develop simultaneously at almost the same time. The pattern of the peaks appears to be repetitive along the domain. The profile continues to rise and the peaks smooth out as the value of $T(t)$ approximately reaches 2.07. Once all the peaks smooth out the profile transforms into a nearly homogeneous form. The sequence of evolution depicted in Fig. 2 (a) (i) – (v) conforms to an almost vertical line in Fig. 2 (c) representing a rapid rise in plastic distortion for a minimal increase in applied stress. The profile retains its nearly homogenous form and rises uniformly during the remainder of the simulation as the applied stress increases to a value of 3.0. This phenomenon is denoted by an inclined straight line in Fig. 2 (c). These plots demonstrate that this model is capable of producing spatial microstructure but stick-slip behavior is not predicted.
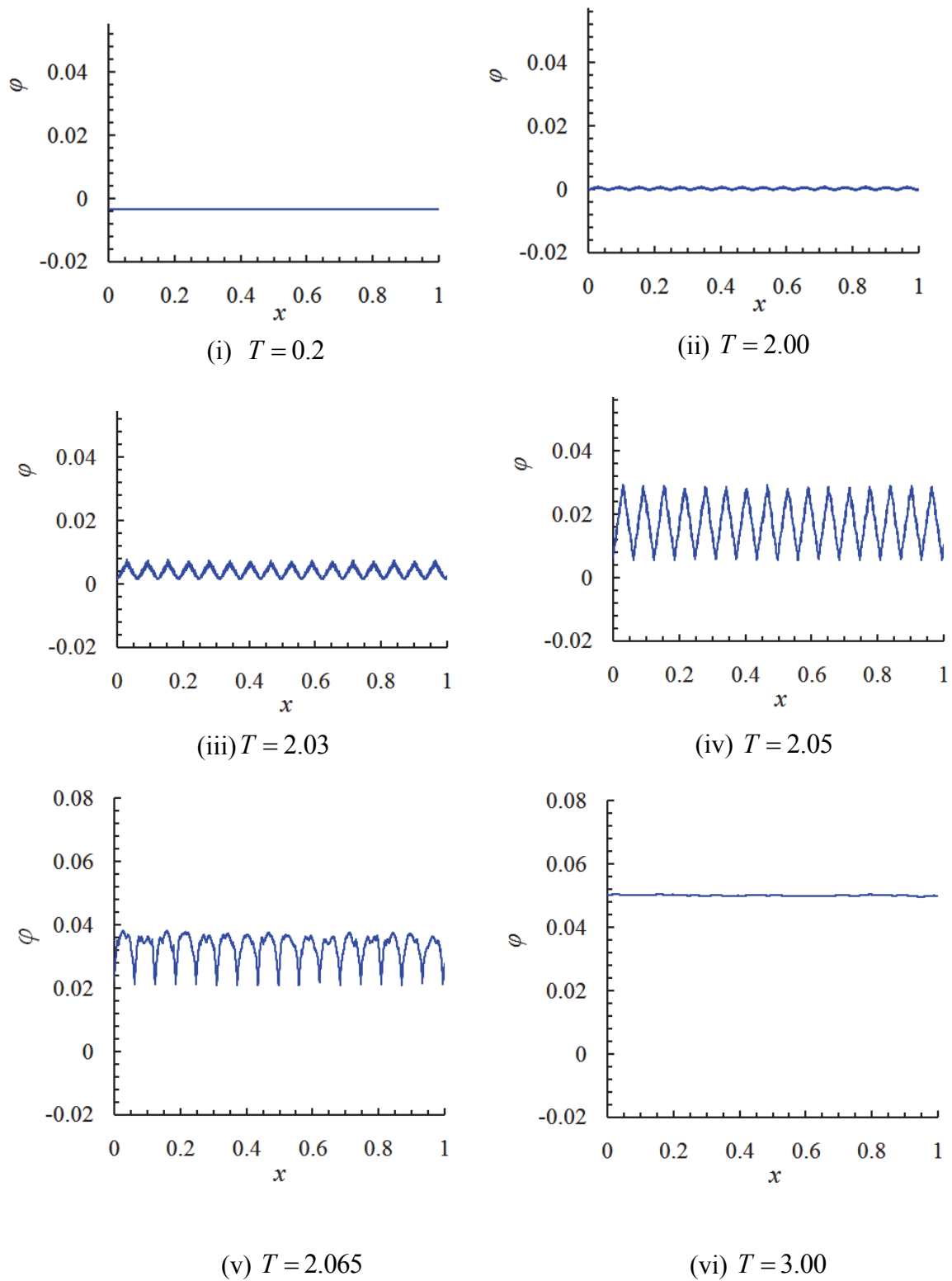
(i) $T = 0.2$

(ii) $T = 2.00$

(iii) $T = 2.03$

(iv) $T = 2.05$

(v) $T = 2.065$

(vi) $T = 3.00$

Fig. 2 (a) Evolution of φ for the model with dislocation
transport, wiggly back stress, and gradient hardening (Case I)

14

(i) $T = 0.2$

(ii) T = 2.0

(iii) $T = 2.03$

(iv) $T = 2.05$

(v) $T = 2.065$

(vi) $T = 3.00$
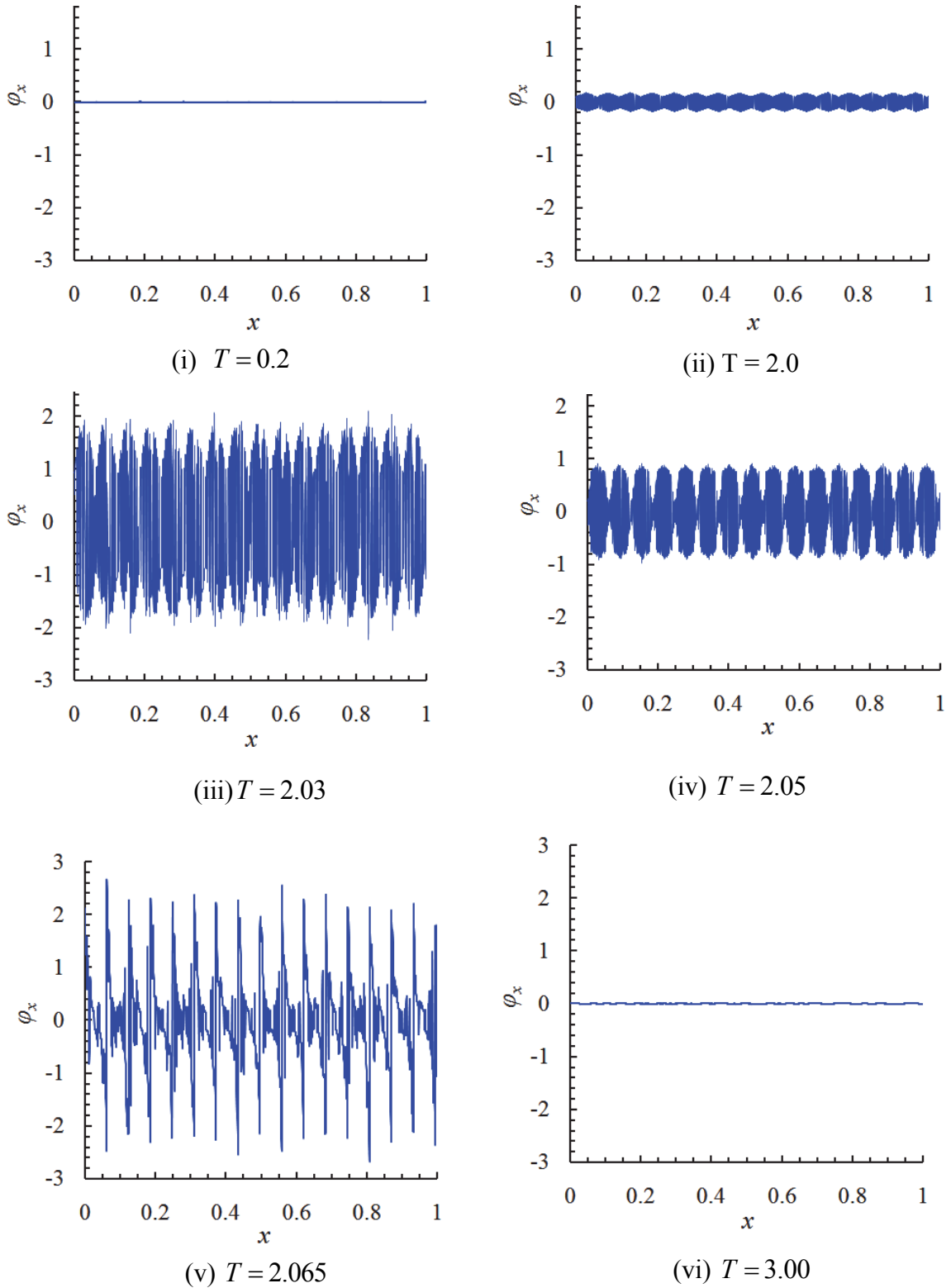
Fig. 2 (b) Evolution of φ_x for the model with dislocation transport, wiggly back stress, and gradient hardening (Case I)
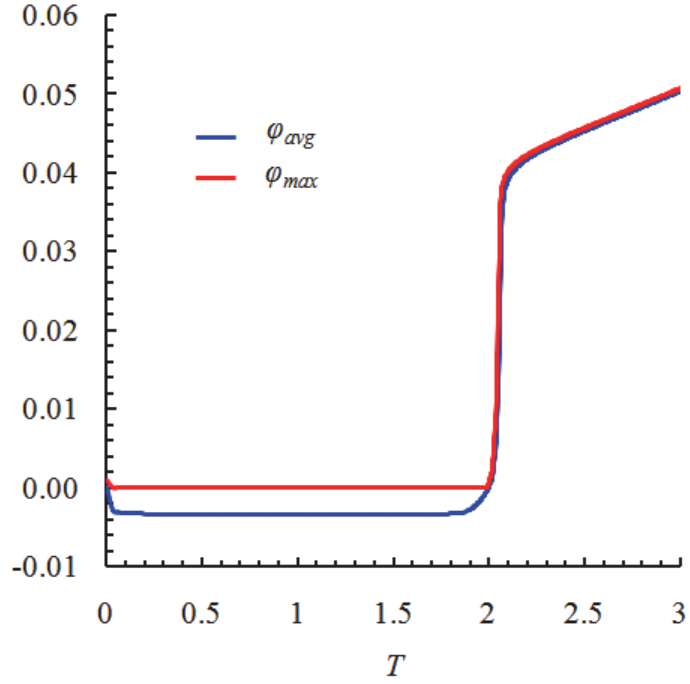
Fig. 2 (c) Variation of spatial average and maximum values of φ with applied load (Case I)

As we shall see in Section 3, the simulations presented in Figure 2 (a-c) above for the parameter values mentioned do not produce converged results with respect to mesh refinement - the reliable conclusion that can be drawn from the specific simulation shown is the appearance of microstructures, but not the specific microstructure itself. However, this is simply a feature of the parameter regime we are operating in (close to the macroscopic limit) and not any specific ill-posedness associated with the model (or the numerical scheme) in more moderate circumstances corresponding to smaller domain sizes in comparison to the interatomic distance. A simulation is performed for a reduced wave number in the initial condition, N, equal to 5 and a higher value of ε^*, increased by a factor of 10 from that mentioned in Table 1. The results of the simulation, shown in Fig. 3, indicate the development of inhomogeneity and yield-like behavior. The magnitude of peaks developed in the φ profiles is non uniform across the domain. Stick-slip phenomenon is not predicted. It will be shown later in Section 3 that this setup leads to a better convergence of results as compared to the model setup for larger domain size.

(i) $T = 0.3$

(ii) 2.02

(iii) $T = 2.03$

(iv) $T = 2.05$

(v) $T = 2.065$

(vi) $T = 3.00$

Fig. 3 (a) Evolution of φ for Case I with high ε^* and low N

(i) $T = 0.2$

(ii) $T = 2.01$

(iii) $T = 2.03$

(iv) $T = 2.05$

(v) $T = 2.065$

(vi) $T = 3.00$
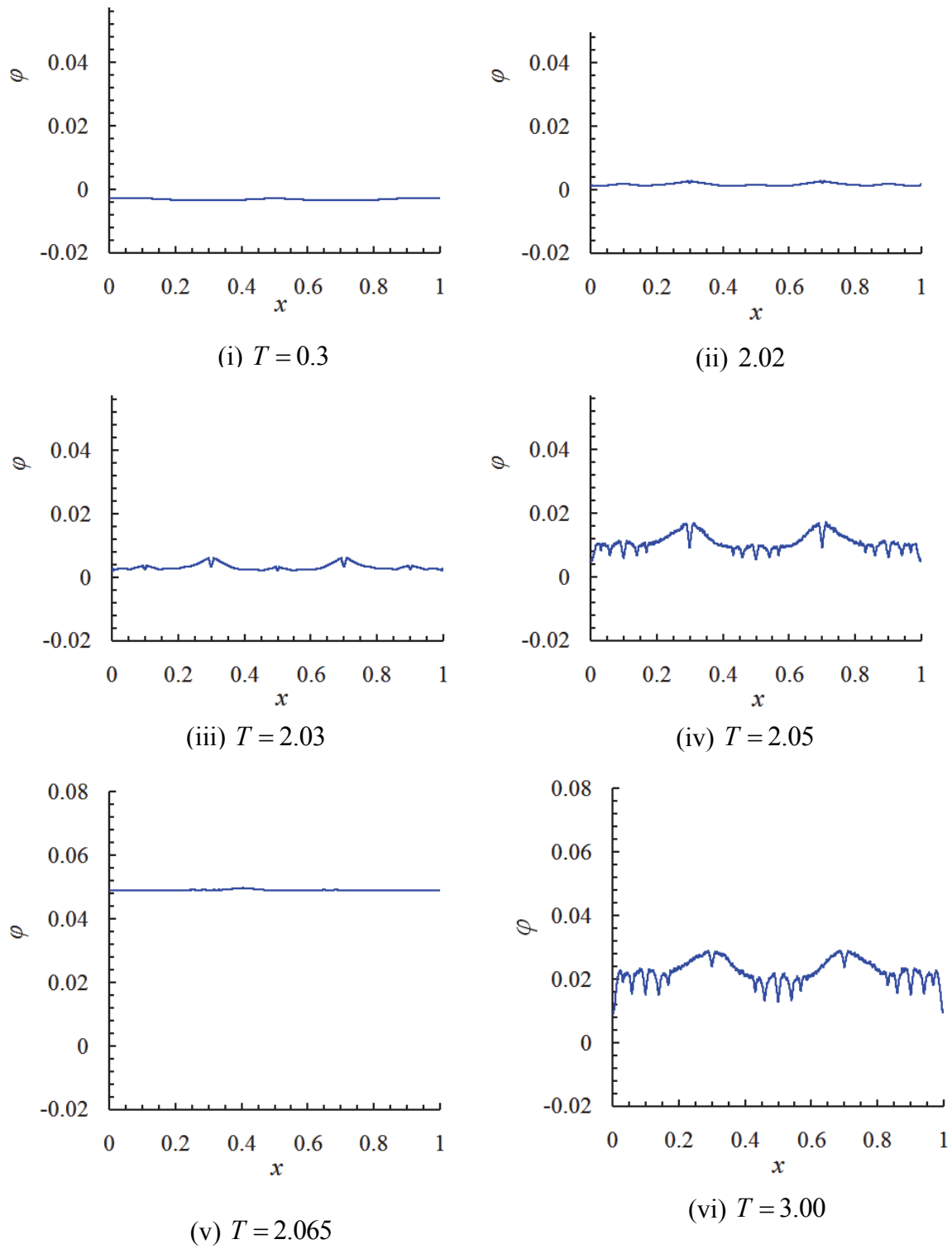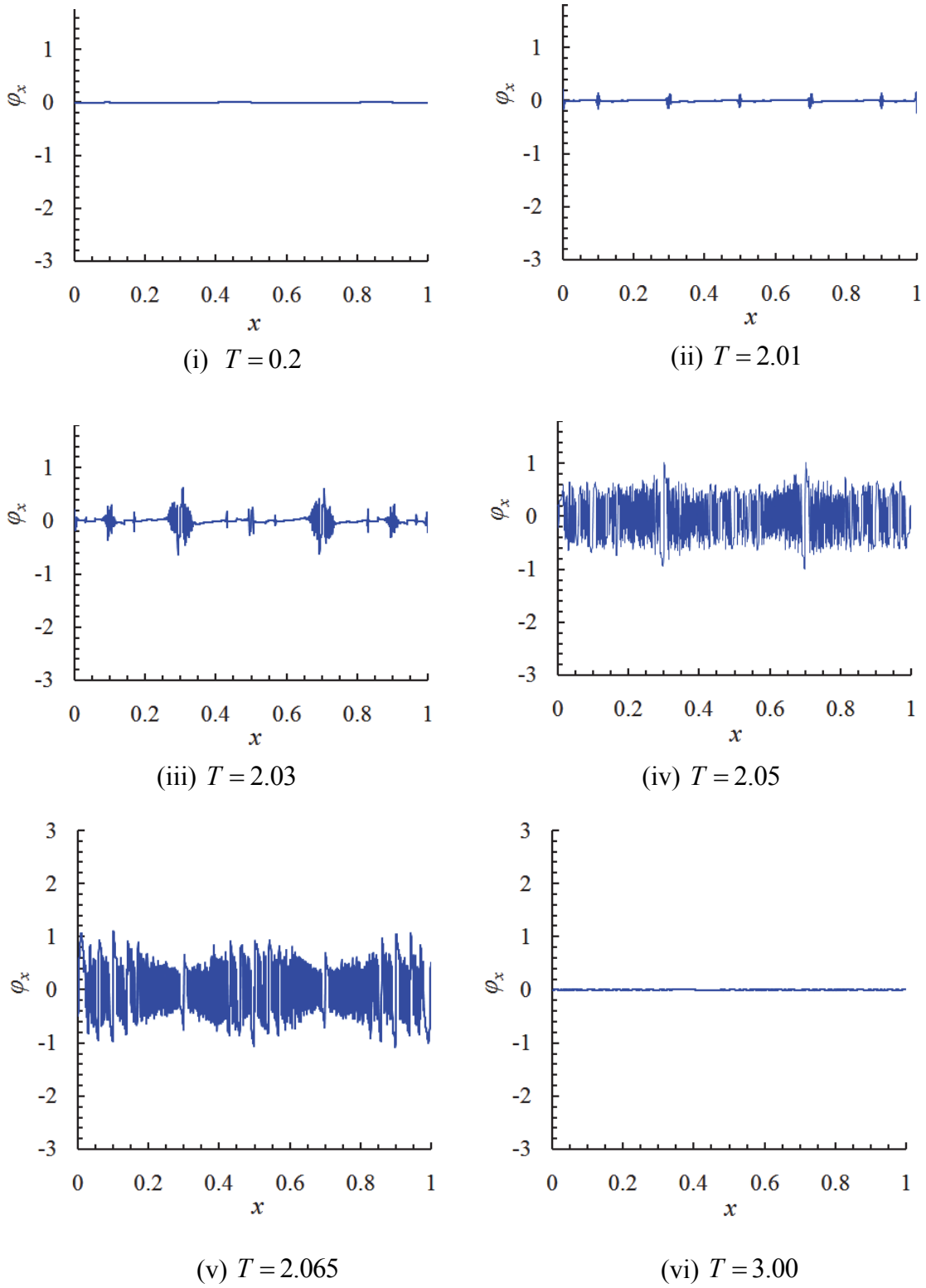
Fig. 3 (b) Evolution of φ_x for Case I
with high ε^* and low N
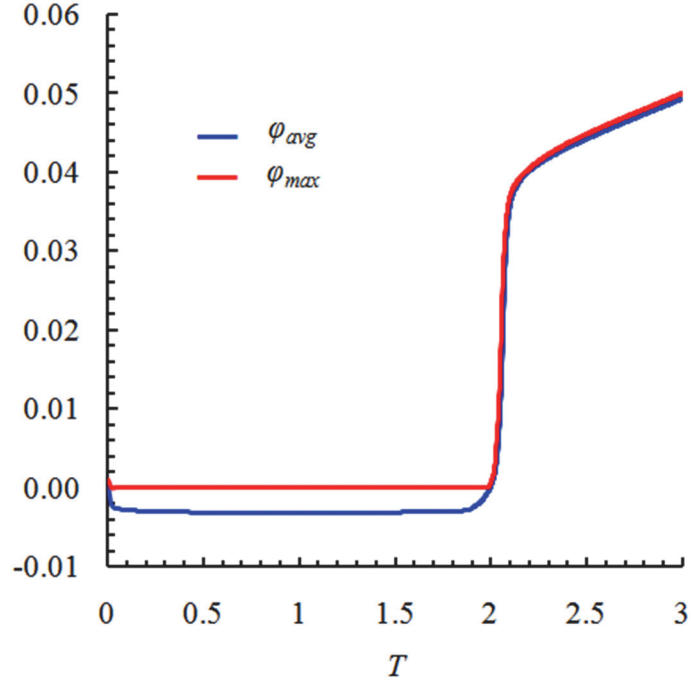
Fig. 3 (c) Variation of spatial average and maximum values of φ with applied load for Case I with high ε^* and low N

2.2. *Case II: Model with dislocation transport, wiggly back stress, and standard hardening*

The model for Case I((20), (23) and (25)) is simulated with $k_0 = 0$. Fig. 3 (a) shows an evolution of the φ profile in this case. The initial φ profile specified by (34) quickly transforms to nearly homogeneous form shown in Fig. 4 (a) (i). This nearly homogenous form is retained until the applied load reaches a value of 2.0 approximately. Sharp peaks, uniformly spaced along the domain, originate almost simultaneously in the profile as shown in Fig. 4 (a) (ii). These peaks spread out leading to formation of a step-like pattern as shown in Fig. 4 (a) (iii), and eventually coalesce with each other as the applied load increases marginally resulting in a nearly homogenous form shown in Fig. 4 (a) (iv).Since the gradient of φ corresponds to dislocation density, the step-like form in the φ profile corresponds to a pair of positive and negative dislocations. This development is indicated by an almost vertical line in Fig. 4 (b) which shows the variation of average and maximum plastic distortion with stress. The subsequent phase of evolution is manifested by a plateau like region in Fig. 4 (b) during which the φ profile remains stationary for an increase in the applied stress levels. As $T(t)$ reaches a value of 2.365 another peak emanates in the profile as shown in Fig. 4 (a) (v). The peak spreads out and forms a step-like pattern in the profile as shown in Fig. 4 (a) (vi) and eventually exits the domain resulting in another nearly homogenous form similar to that shown in Fig. 4 (a) (iv). More peaks develop at apparently random stress levels and locations in the domain as shown in Figs. 4 (a) (vii), (viii) and (ix). The locations of origins of peaks are sensitive to the precise details of the prescribed

19

initial condition up to the level of distinguishing different meshes for the same analytical initial condition. Stick-slip behavior, evident from Fig. 4 (b), is illustrated from these results where a dormant phase (with no plastic growth) is followed by a phase of greater plastic growth (with significant movement and interaction of dislocations) and is again followed by a dormant phase. Overall, the completely deterministic evolution gives an impression of apparently stochastic behavior. The behavior predicted is reminiscent of the propagation of Luders' bands in metals. Given the strong discontinuities, both in space and time, that are predicted, it is highly unlikely to expect any type of convergence in these results with respect to mesh refinement. We present the results simply because of their 'remarkable' nature.
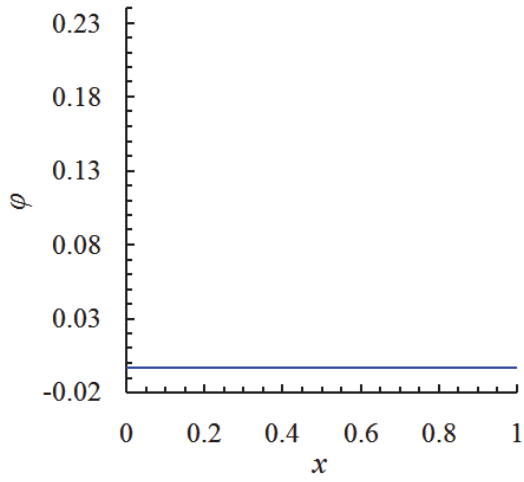
(i) $T = 0.1$
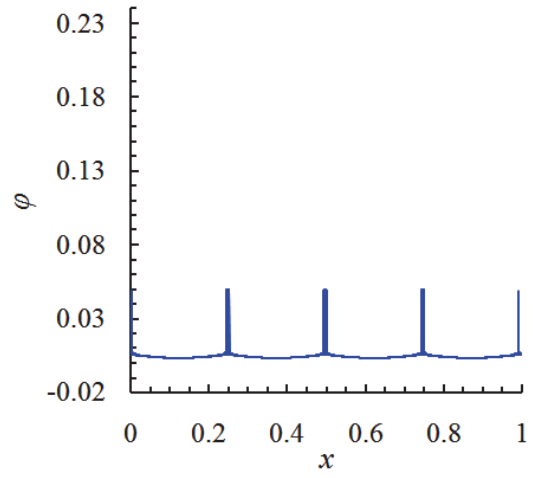
(ii) $T = 2.0189$
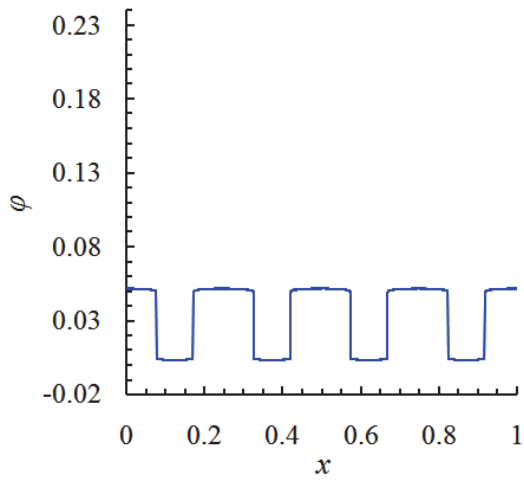
(iii) $T = 2.0190$
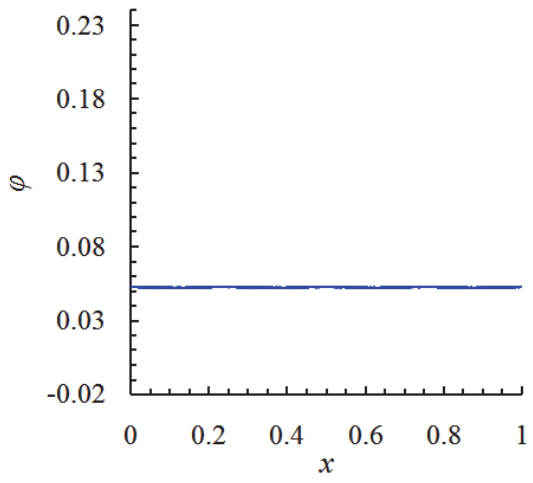
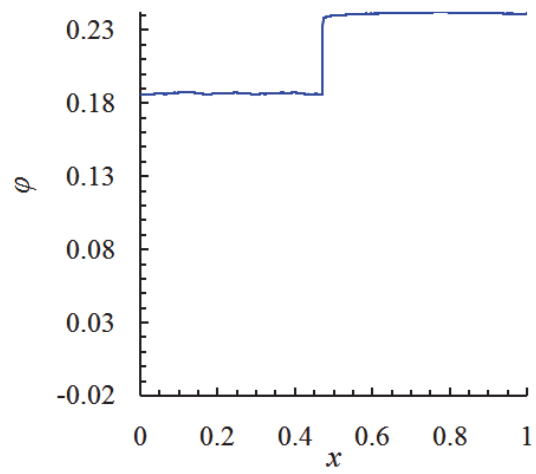(iv) $T = 2.02$
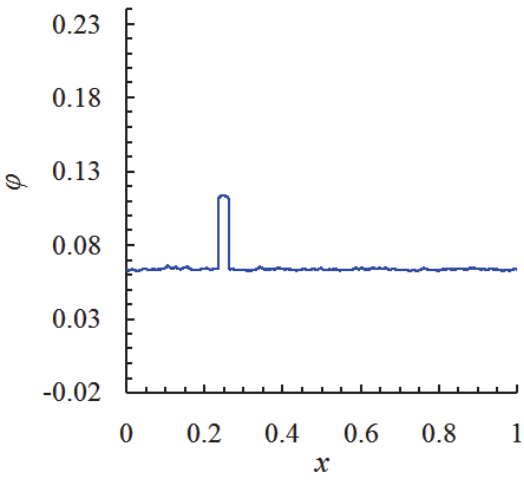
(v) $T = 2.365$
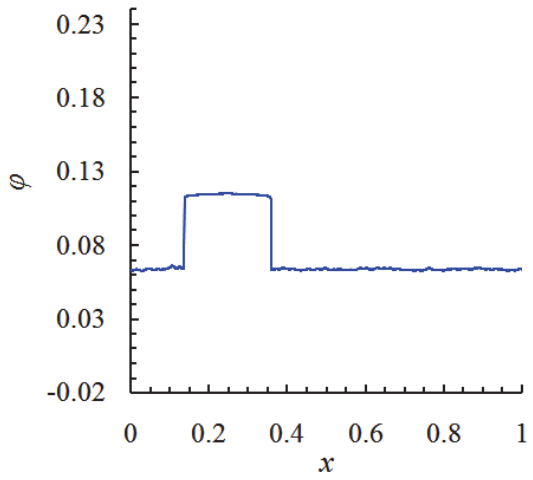
(vi) $T = 2.366$
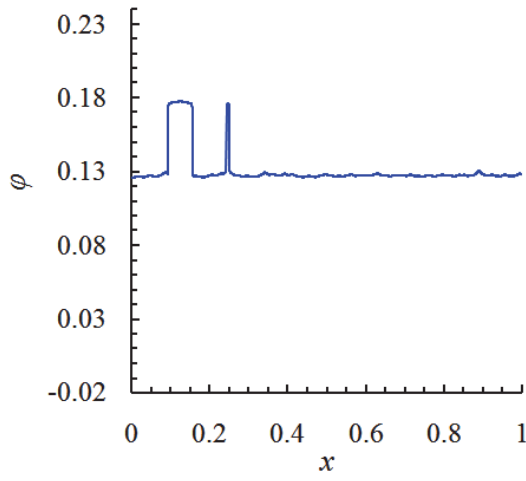
(vii) $T = 2.694$
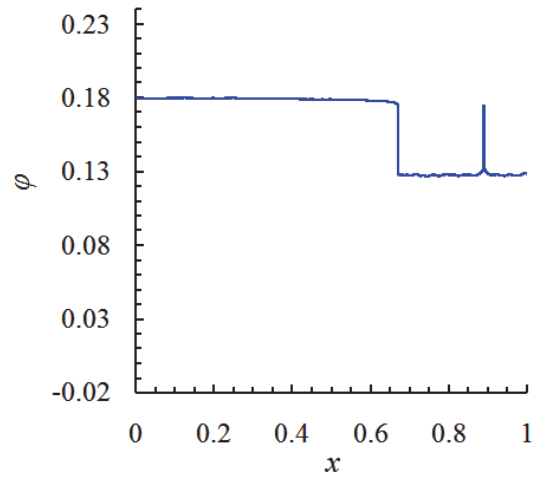
(viii) $T = 2.699$
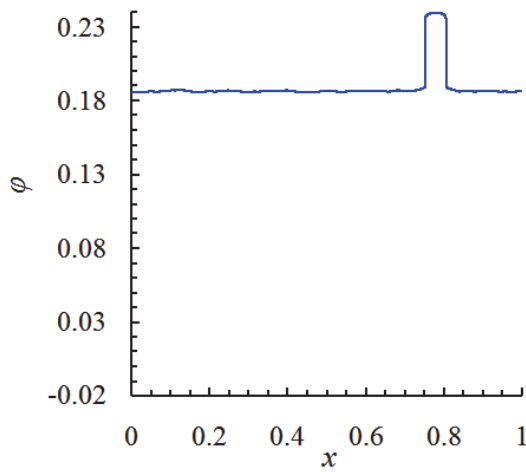
(ix) $T = 2.857$

(x) $T = 2.862$

Fig. 4 (a) Evolution of φ for the model with dislocation transport, wiggly back stress, and standard hardening (Case II).
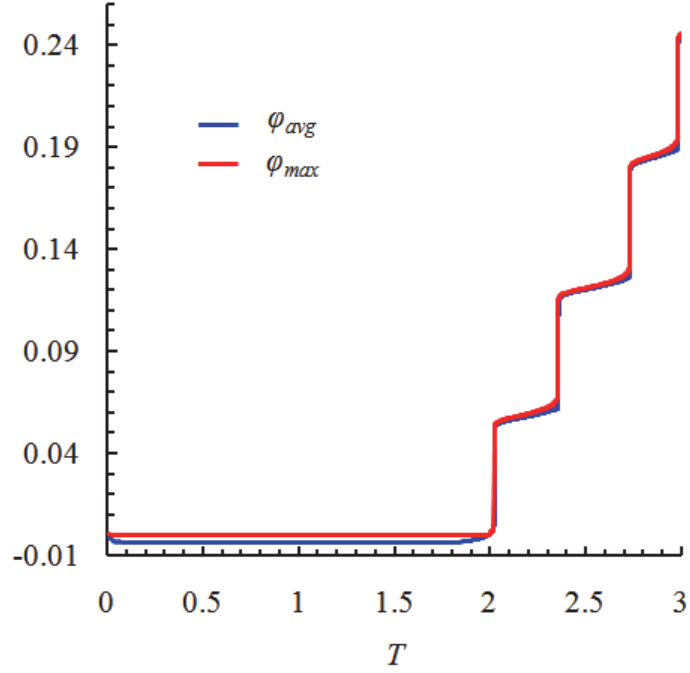
Fig. 4 (b) Variation of spatial average and maximum values of φ
with applied load (Case II)

2.3. *Case III: Model with wiggly back stress, gradient hardening no dislocation transport*

As already stated in the Introduction (Section 1), the plastic strain-rate consists of two parts, one produced by the motion of dislocation density fields reflected in (5) by $-\varphi_x V$, plus that due to the motion of the unresolved statistical dislocations modeled by L^p. In this section, we investigate a different model for the first part of the strain-rate, assuming that it does not result from transport, but rather is governed by the thermodynamic force $-\delta\psi/\delta\varphi$. A constitutive relation must be prescribed for this part of the strain-rate, replacing the kinetic relation (10) for V, and this is done by assuming a simple linear dependence on the thermodynamic force. The resulting set of equations used in the simulations is

$$\varphi_t = \frac{1}{B}\left[T - \frac{\partial G}{\partial \varphi} + \varepsilon\varphi_{xx}\right] + \left(\frac{\left|T - \frac{\partial G}{\partial \varphi}\right|}{g}\right)^{\frac{1}{m}} \operatorname{sgn}\left(T - \frac{\partial G}{\partial \varphi}\right),$$

$$(36)$$

$$g_t = \left(\frac{\left|T - \frac{\partial G}{\partial \varphi}\right|}{g}\right)^{\frac{1}{m}}\left[k_0\left|\varphi_x\right| + \theta_0\left(\frac{g_s - g}{g_s - 1}\right)\right].$$

Note that these equations are apparently similar to (11)-(12), with the noticeable difference that there is no transport term $\left|\varphi_x\right|$ in the first term on the right-hand side of $(36)_1$.

Figure 5(a) shows the evolution of the φ profiles in time. Although a yield-like behavior similar to that in Fig. 2 (c) is observed the yielding happens comparatively earlier when the applied stress is approximately equal to 1.2. This is because the extra plastic strain rate term (i.e. the first term on the right-hand side of $(36)_1$) is active without a yield threshold and even in the presence of homogeneous plastic strain. After yielding, the profile begins to move upwards and there is no development of peaks in the φ profile. Hence, in the absence of dislocation transport in plastic strain rate, there is neither a development of large scale inhomogeneity nor a formation of ideal microstructure. Fig. 5 (b) shows the variation of spatial average and maximum values of φ with applied load. The wavy nature of the slope after yielding in these plots suggests the presence of stick-slip behavior.
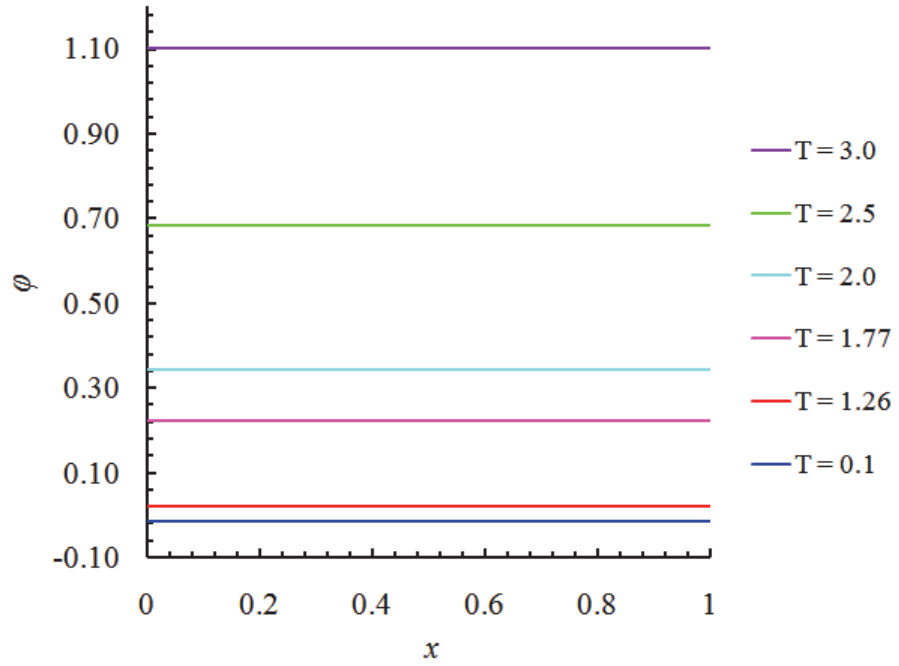
Fig. 5 (a) Evolution of φ for the model with wiggly back stress, gradient hardening but no dislocation transport (Case III)
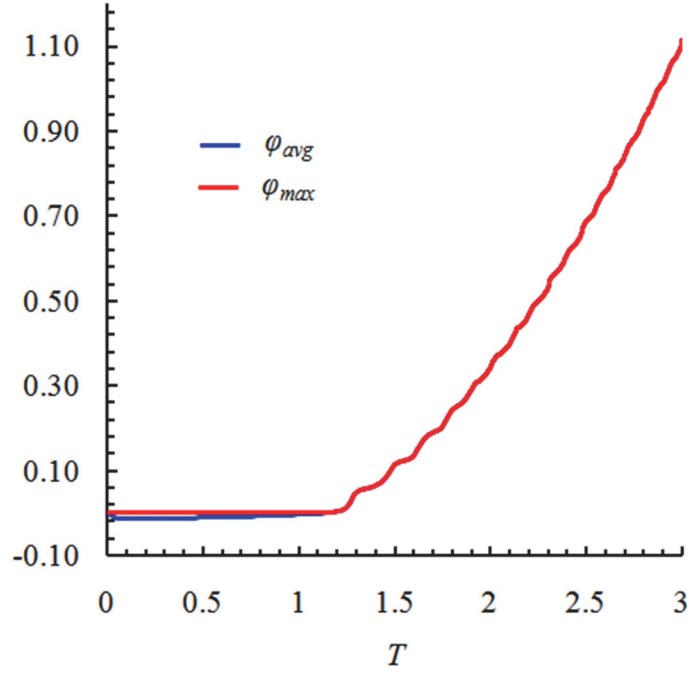
Fig. 5 (b) Variation of spatial average and maximum
values of φ with applied load (Case III)

2.4. *Case IV: Microstructure due to dislocation transport and gradient hardening with no non-monotone equations of state*

Fig. 6 (a) is a plot of the evolution of φ when the wiggly back-stress term is set to be equal to zero. The model is:

$$\varphi_t = \frac{|\varphi_x|}{B}[T + \varepsilon\varphi_{xx}] + \left(\frac{T}{g}\right)^{\frac{1}{m}}, \qquad T \geq 0,$$

$$g_t = \left(\frac{T}{g}\right)^{\frac{1}{m}}\left[k_0|\varphi_x| + \theta_0\left(\frac{g_s - g}{g_s - 1}\right)\right].$$

$$(37)$$

Development of inhomogeneous profiles is observed. Fig. 6 (d) shows the variation of spatial average and maximum values of φ with applied load. No stick-slip behavior is observed. Figs. 6 (b) (ii) – (vi) show the φ_x profiles that clearly demonstrate the dislocation microstructure that develops. Dense dipolar walls of positive and negative dislocations separated by spatially non-periodic 'cell-like' regions of relatively sparse dislocations density are observed. This microstructure bears some superficial similarity to the persistent slip-band microstructures that are observed in fatigue experiments (Mughrabi, Ackerman and Herz, 1979). A magnified view, shown in the section plots of Fig. 6 (c), suggests that

26

the φ_x profile is continuous which in turn implies that the plastic distortion is smooth in this case.

Fig. 6 (c), and the dynamic simulation associated with it, shows that even in this relatively (physically) simple model, three separated distinguished microstructural length scales emerge, that appear to evolve in time. The first is at the scale of the core width $(\sim b)$ as can be seen from the zoomed in view. Second is the width of the dense dislocation walls. The third microstructural length scale is the cell-size (regions of low dislocation density content). In all three cases there does not appear to be a fixed value for each length, but rather they vary in space and time. We think that these lengths are related to the nondimensional parameters ε^*, B^*, and k_0^*, and suspect that there are asymptotic scaling laws to be uncovered (cf. Barenblatt, 1996) in this context.
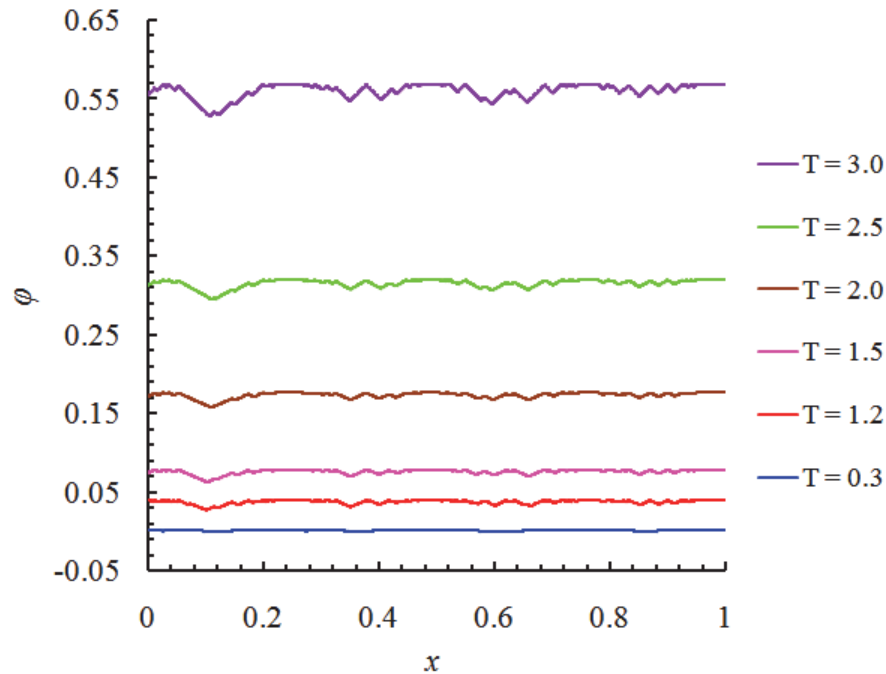

Fig. 6 (a) Evolution of φ for the model with dislocation transport and gradient hardening without non-monotone equations of state (Case IV)
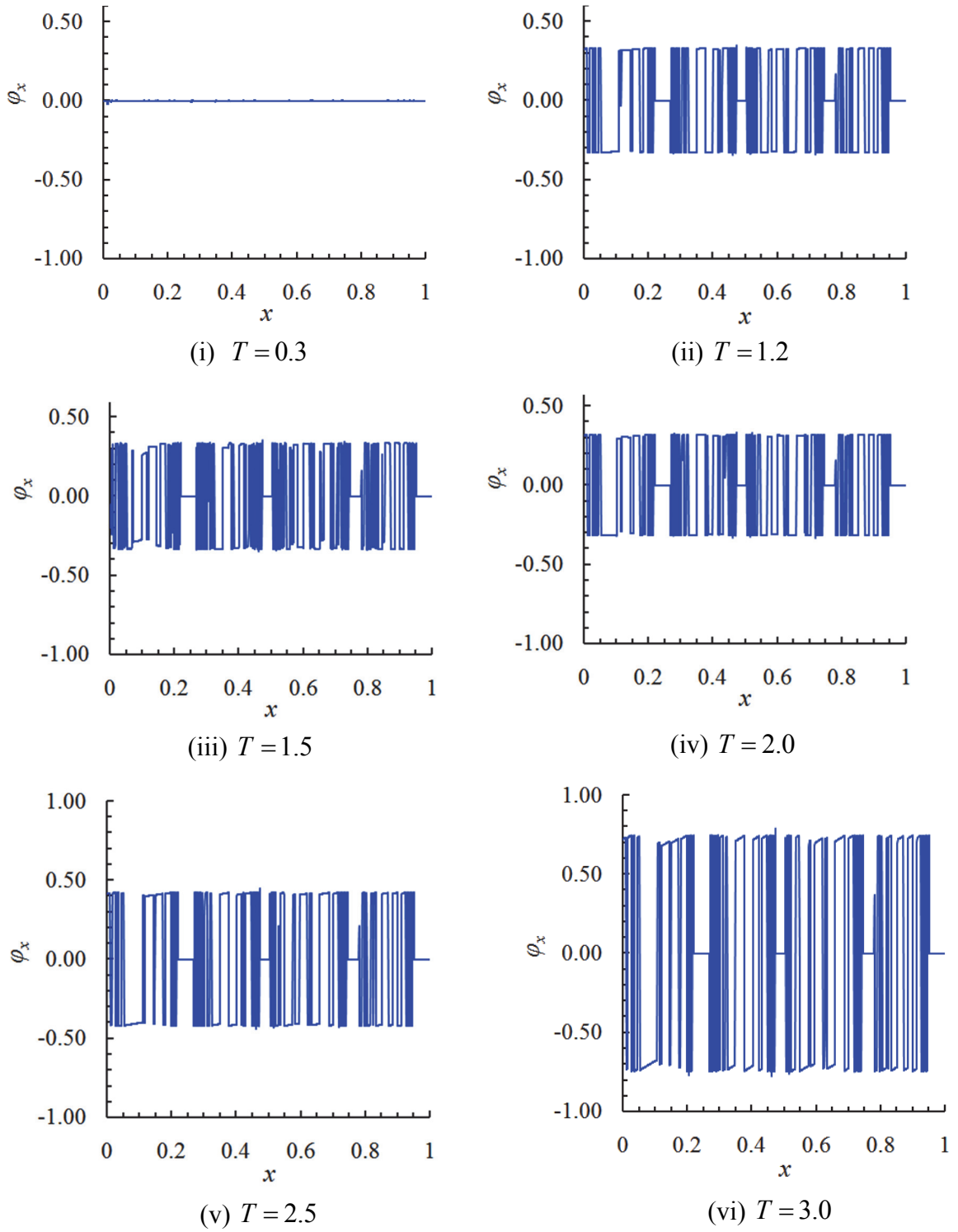
(i) $T = 0.3$ (ii) $T = 1.2$

(iii) $T = 1.5$ (iv) $T = 2.0$

(v) $T = 2.5$ (vi) $T = 3.0$

Fig. 6 (b) Evolution of microstructure due to dislocation transport
without non-monotone equations of state (Case IV)
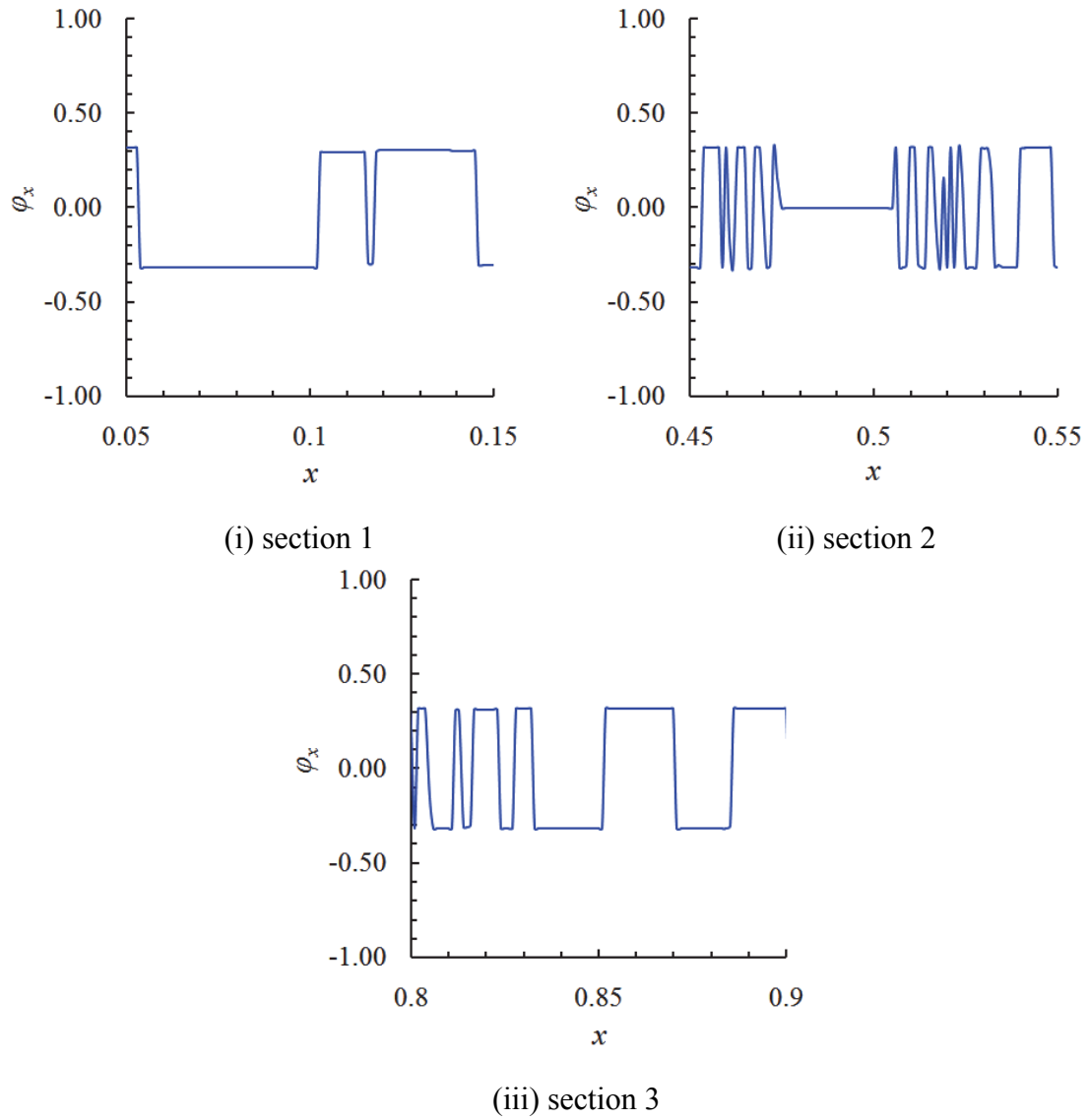
(i) section 1   (ii) section 2

(iii) section 3

Fig. 6 (c) Sections of microstructure developed at stress level $T = 1.5$ (Case IV)
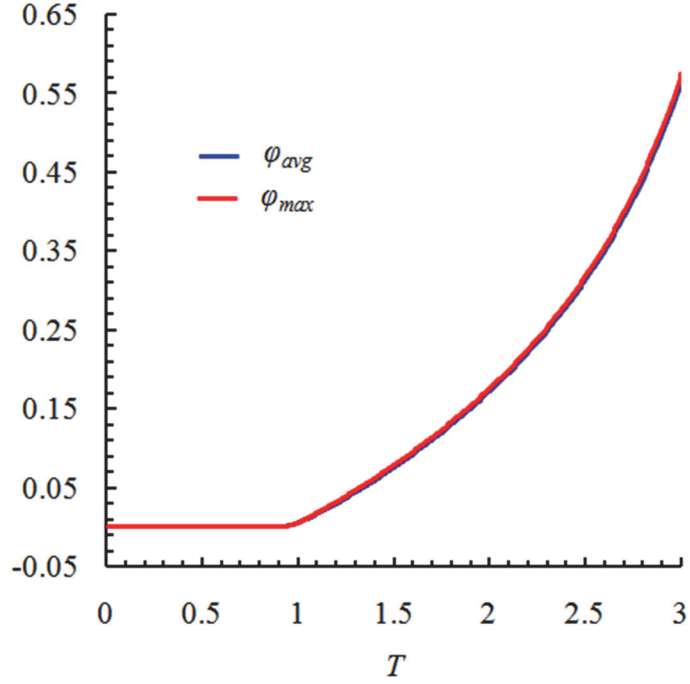
Fig. 6 (d) Variation of spatial average and maximum values
of φ with applied load (Case IV)

It is possible to provide some mathematical understanding of the emergence of inhomogeneity in this case. Equation (37) is a degenerate, quasi-linear parabolic system that results in a nonlinear (not quasi-linear) first-order system of pde in g and $\alpha = \varphi_x$ for $\varepsilon = 0$, i.e. in the absence of core energy. The principal part of the linearization of this first-order system belongs to the class analyzed in Sec. 4.2.1 of Roy and Acharya (2006). It was shown there that the problem is only weakly-hyperbolic (real eigenvalues, but not a full set of eigenvectors) when linearized about a homogeneous plastic strain profile, the case of interest here. As is known, weakly hyperbolic systems are unstable (Kreiss and Lorenz, 1999), and it is no surprise then that we see growth of perturbations. We note that the degeneracy of the parabolic regularization in our problem allows the principal part of the first-order problem to remain intact for linearization about the homogeneous plastic strain state. Thus, *development of inhomogeneity is expected to be a generic feature of our model, unrelated to non-monotone equations of state.* What the linear analysis does not say anything about is the long-time response of the growing perturbations, and our calculations here provide yet another confirmation of the conjecture in Roy and Acharya (2006) that because of the stabilizing feedback, through hardening due to the increase in $|\alpha|$, the instability should be controlled. Perhaps more convincing is the fact that we have the degenerate parabolic regularization due to the core energy for $\varepsilon > 0$ in (37) which provides particularly strong diffusive regularization in any region of sharp gradients in φ (due to the multiplication by $|\varphi_x|$), and therefore the φ solutions of the model may be generically expected to remain smooth and α bounded. We remark that in problems where a system with more than one plastic strain component is involved, it is known that, at least in 1

30

spatial dimension and time, the system is weakly hyperbolic without core regularization even without any involvement from hardening (Acharya and Tartar, 2011), and again the development of microstructure is to be expected (cf. Chen et al., 2013).

2.5.*Case V: Model with dislocation transport standard hardening with no non-monotone equations of state*

Fig. 7 (a) is a plot of the evolution of φ when the wiggly back-stress term and k_0 is set to be equal to zero. The model is:

$$\varphi_t = \frac{|\varphi_x|}{B}[T + \varepsilon\varphi_{xx}] + \left(\frac{T}{g}\right)^{\frac{1}{m}}, \qquad T \geq 0,$$

$$g_t = \left(\frac{T}{g}\right)^{\frac{1}{m}}\left[\theta_0\left(\frac{g_s - g}{g_s - 1}\right)\right].$$

(38)

There is no development of inhomogeneity in the φ profile for this model. A yield-like behavior is observed at a stress level equal to 1.0. After yielding the spatial average and maximum values of φ vary nonlinearly with applied load as shown in Fig. 7 (b).In this model, the second equation is uncoupled from the first and the evolution of φ becomes that of a scalar equation with a time dependent forcing.
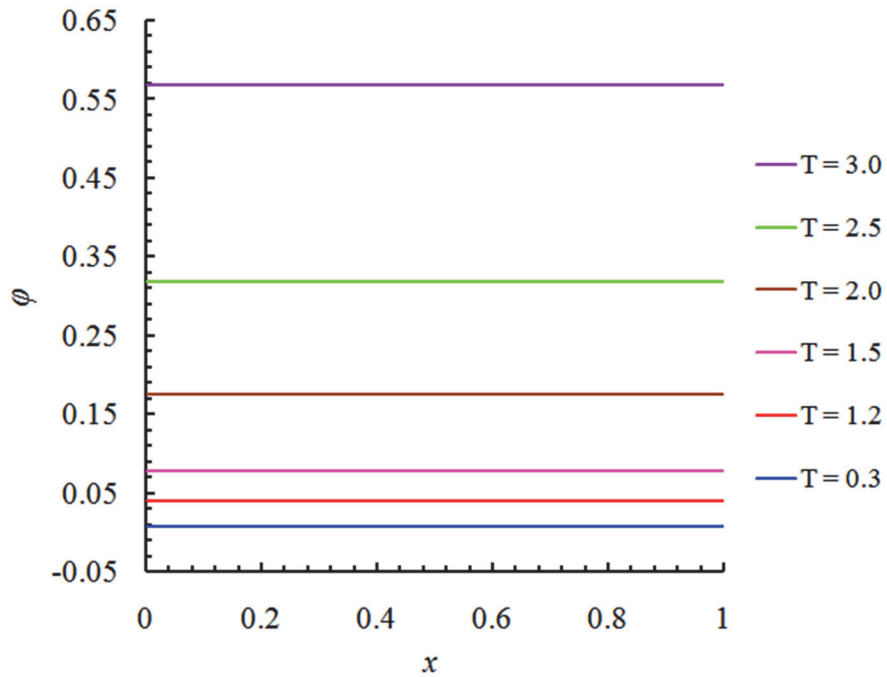

Fig. 7 (a) Evolution of φ for the model with dislocation transport, standard hardening and no non-monotone equations of state (Case V)
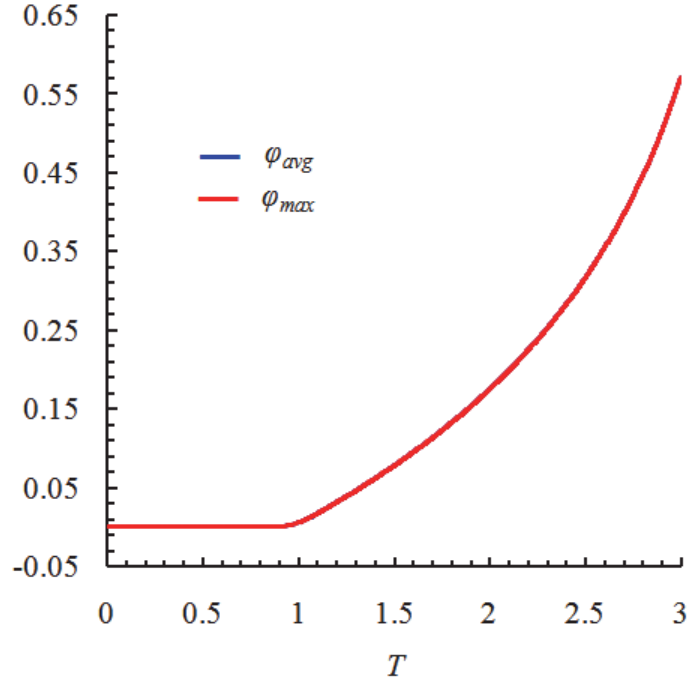
31

Fig. 7 (b) Variation of spatial average and maximum
values of φ with applied load (Case V)

2.6. *Case VI: Conventional plasticity*

The conventional plasticity model can be simulated using the following equations:

$$\varphi_t = \left(\frac{T(t)}{g}\right)^{\frac{1}{m}} \quad ; \quad T(t) \geq 0$$

$$g_t = \left(\frac{T(t)}{g}\right)^{\frac{1}{m}} \left[\theta_0\left(\frac{g_s - g}{g_s - 1}\right)\right].$$

(39)

The result of the simulation performed using (39) is shown in Fig. 8 (a). The applied loading increases uniformly from 0 to 3. The form of the initial φ profile is retained during the entire simulation. A yield like behavior is observed where the profile remains stationary until the applied load reaches 0.95 and rises with further increase in loading. There is no development of large-scale inhomogeneity in the φ profile. The φ_x profiles appear to be stationary as shown if Fig. 8 (b). Fig. 8 (c) shows the variation of spatial average and maximum values of φ with applied load. A yield like behavior is observed but stick-slip behavior is absent.
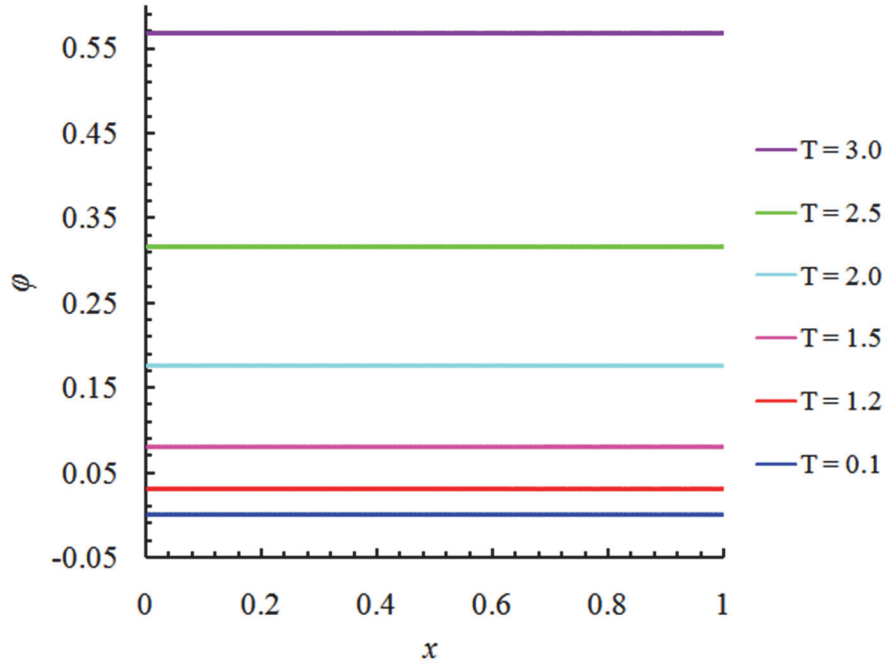
32

Fig. 8 (a) Evolution of φ for the conventional plasticity model (Case VI)
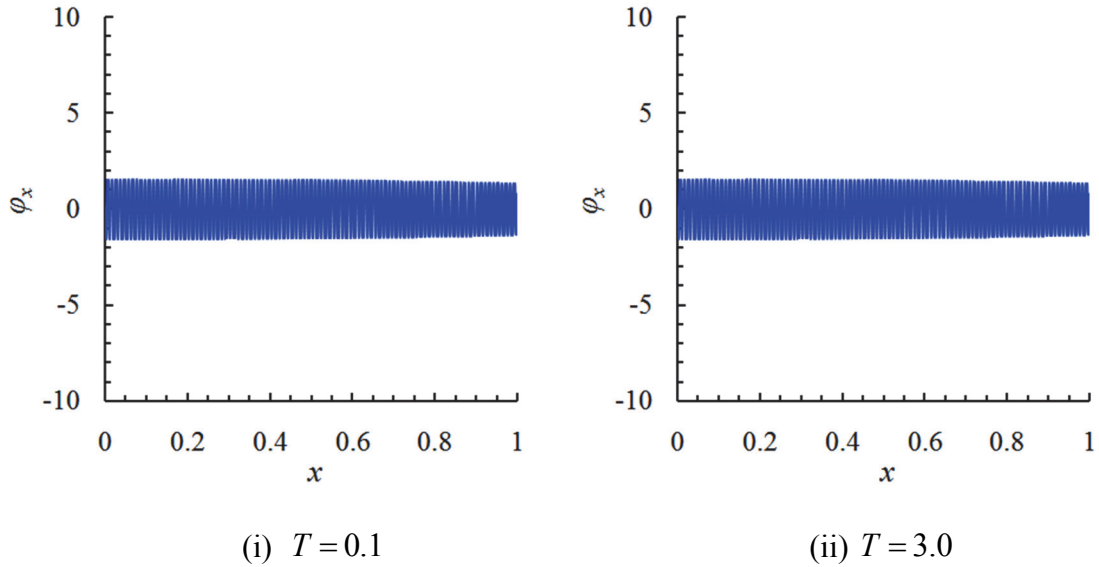

(i) $T = 0.1$ (ii) $T = 3.0$

Fig. 8 (b) Evolution of φ_x for the conventional plasticity model (Case VI)
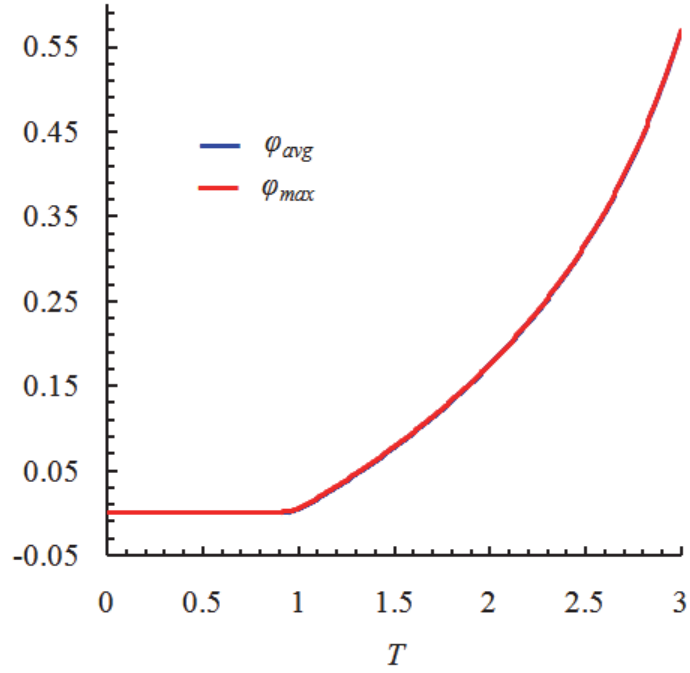
Fig. 8 (c) Variation of spatial average and maximum
values of φ with applied load (Case VI)

3. Limit of the models corresponding to macroscopic scales of observation

The constitutive model (11)-(12) contains a small parameter ε which measures the intensity of the core energy and, as explained in the discussion surrounding (22), its non-dimensional counterpart ε^* also measures the length scale of observation with respect to the interatomic distance. This core energy plays a (physical) regularizing role in that it helps to spread the plastic distortion φ and avoids singularities in its gradient. However, when observed at large macroscopic scales, such smooth but large gradients appear as discontinuities. The objective of this section is to investigate, numerically, the behavior of the different models as the nondimensional parameter ε^* goes to 0.

A careful inspection shows that there are at least 3 small parameters at play in the computed response of the different models. In addition to the parameter ε^*, the other parameters are the wavelength of the initial condition (34), $\lambda = \dfrac{1}{N}$, and the spatial discretization $d = x_h - x_{h-1}$.

We first discuss the effect of mesh refinement on the results obtained from the model governed by ((20), (23),(25)), i.e. Case I. A set of simulations is performed with three meshes of 10000, 20000 and 40000 elements for the initial condition prescribed by (34)

for a wave number in the initial condition $N = 5$ and a value of ε^* increased by a factor of 10 from that mentioned in Table 1. The results of these simulations are shown in Fig. 9 (a). The resulting profiles for different mesh sizes have similar form and it can be considered that convergence with the mesh size is attained at a rather coarse mesh size.

Next we consider the macroscopic limit which corresponds to $\varepsilon^* \ll 1$ as given in Table 1 and a high wave-number initial condition of $N = 500$. Simulations are again performed with the three different meshes. Evolution of the φ profile for different mesh sizes is shown in Fig. 9 (b). A lack of convergence is observed, particularly between stress levels 2.0 and 2.1 when inhomogeneity develops in the profile. A comparatively higher number of peaks develop in the profile for the simulation performed with a finer mesh. Two conclusions can be drawn from these observations. First, for the parameters considered, a very fine mesh is required in order to obtain converged results with respect to the mesh size, if at all.

The second conclusion is that solutions become highly oscillatory when ε^* becomes small, a situation reminiscent of that of homogenization (Tartar, 2009), or wiggly energies (Abeyaratne et al., 1996). Therefore a careful mathematical analysis of the weak limits of these solutions is required in order to derive the "effective" equations governing the evolution of the system in the limit as ε^* goes to 0. This is beyond the scope of the present paper.

Next we perform the same test in the macroscopic limit for the model described in Case IV governed by (37) with ε^* as specified in Table 1 and $N = 500$. The comparison of results obtained with different meshes in shown in Fig. 9(c). The absence of non-monotone equations of state in the model leads to good convergence even for a high wave number initial condition.

To quantify the differences in the results for different meshes the following error measures are computed.

$$\xi(\varphi)^{40K-20K} = \frac{2\sqrt{\int_L \left(\varphi^{40K} - \varphi^{20K}\right)^2 dx}}{\left(\sqrt{\int_L \left(\varphi^{40K}\right)^2 dx} + \sqrt{\int_L \left(\varphi^{20K}\right)^2 dx}\right)}$$

$$\xi(\varphi)^{20K-10K} = \frac{2\sqrt{\int_L \left(\varphi^{20K} - \varphi^{10K}\right)^2 dx}}{\left(\sqrt{\int_L \left(\varphi^{20K}\right)^2 dx} + \sqrt{\int_L \left(\varphi^{10K}\right)^2 dx}\right)},$$

(40)

where φ^{10K}, φ^{20K} and φ^{40K} denote the φ values obtained using a mesh of 10000, 20000 and 40000 elements, respectively. $\xi(\varphi)^{40K-20K}$ denotes the error for comparison between φ values for meshes of 40000 and 20000 elements. Likewise, $\xi(\varphi)^{20K-10K}$ is the error for comparison between φ values for meshes of 20000 and 10000 elements. The variation of error with applied stress is shown in Fig. 10. These figures are consistent with the

corresponding plots shown in Fig. 9. The error values are smaller for Case IV and Case I (Fig. 9(a)) as compared to Case I (Fig. 9(b)).
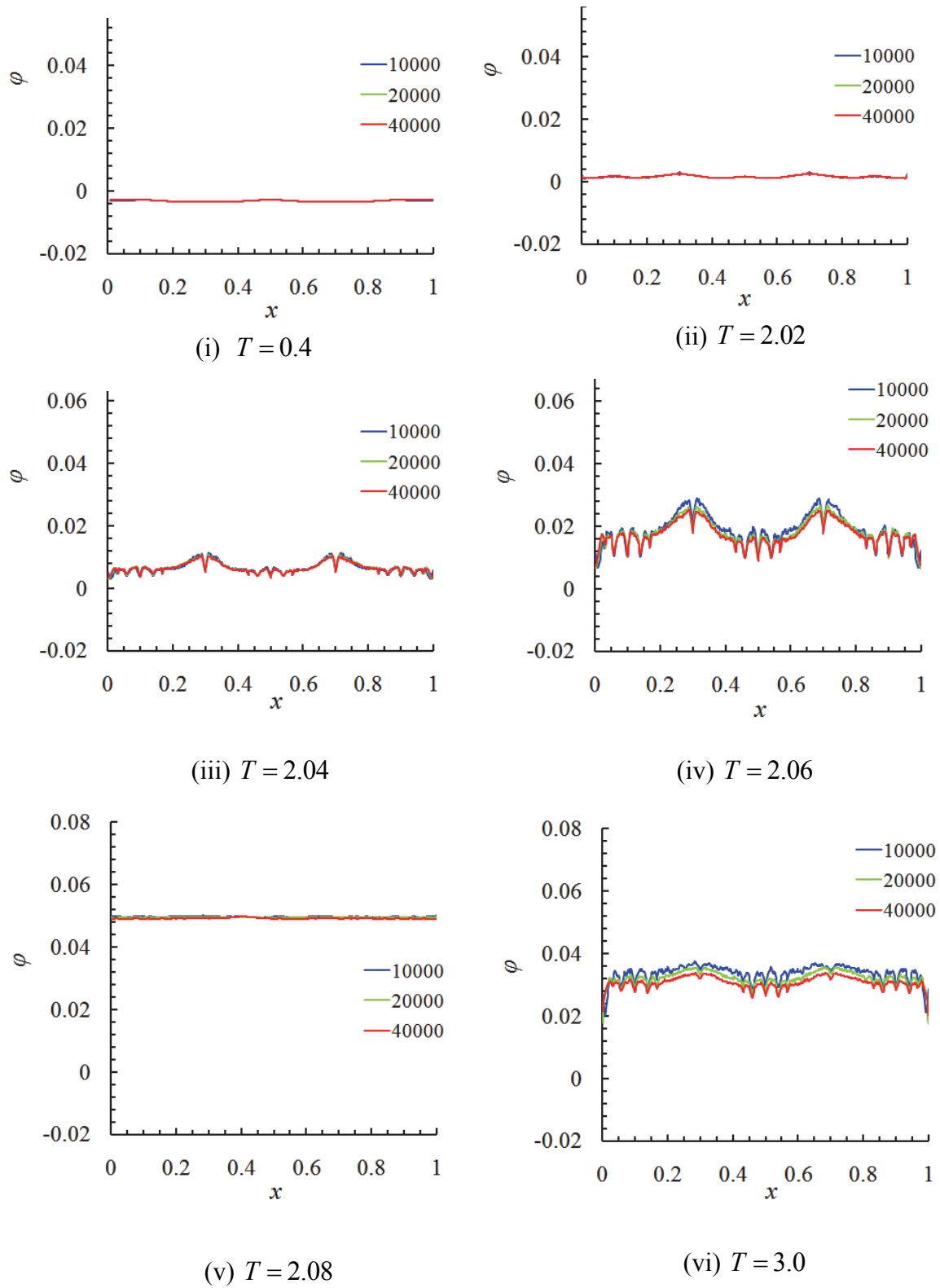
(i) $T = 0.4$

(ii) $T = 2.02$

(iii) $T = 2.04$

(iv) $T = 2.06$

(v) $T = 2.08$

(vi) $T = 3.0$

Fig. 9 (a) Convergence of φ evolution for Case I with high value of ε^* and low N

(i) $T = 0.4$

(ii) $T = 2.02$

(iii) $T = 2.04$

(iv) $T = 2.06$

(v) $T = 2.08$

(vi) $T = 3.0$
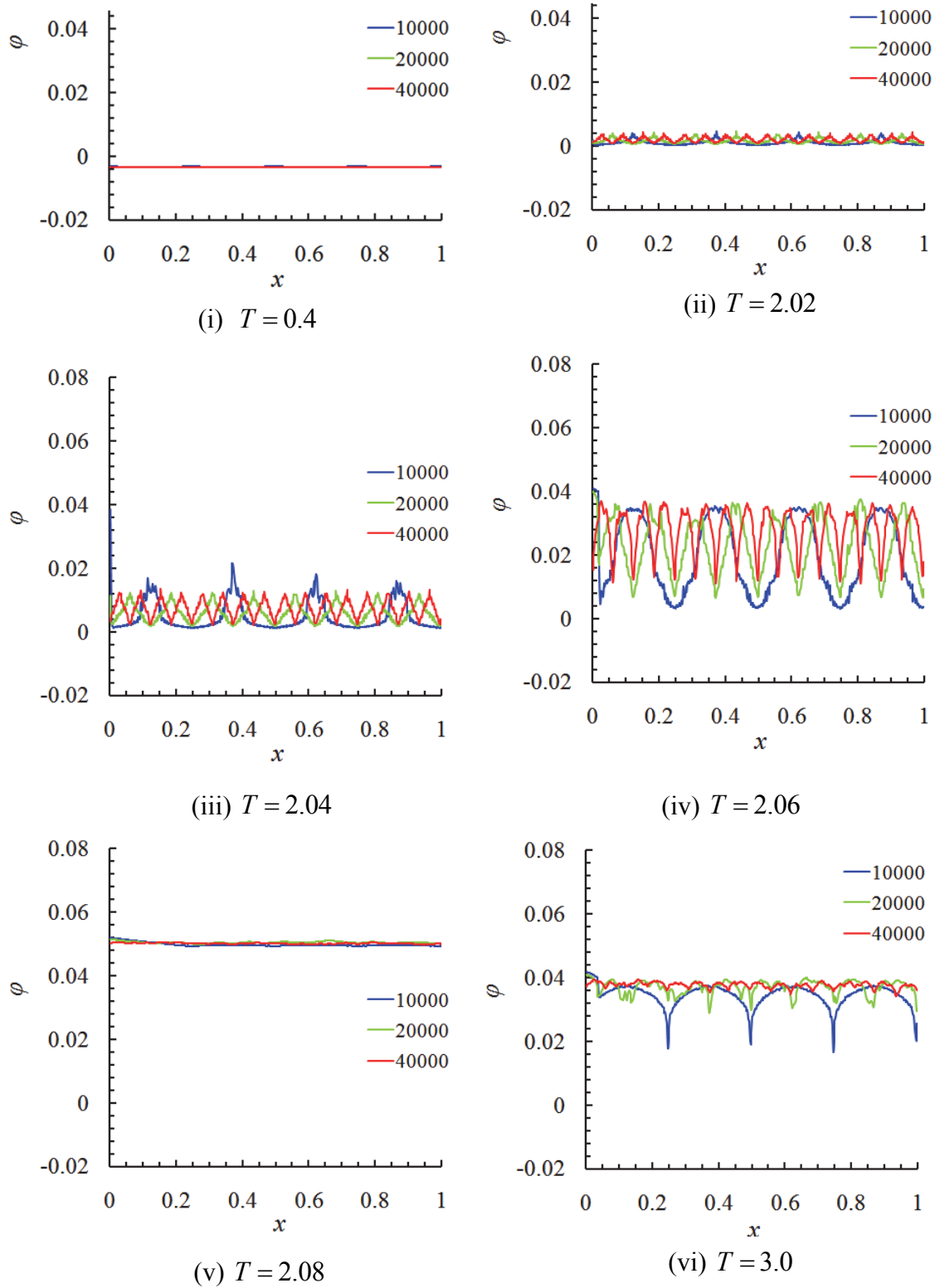
Fig. 9 (b) Lack of convergence of φ evolution for Case I
for low ε^* and high N

(i) $T = 0.3$

(ii) $T = 1.2$

(iii) $T = 1.5$

(iv) $T = 2.0$
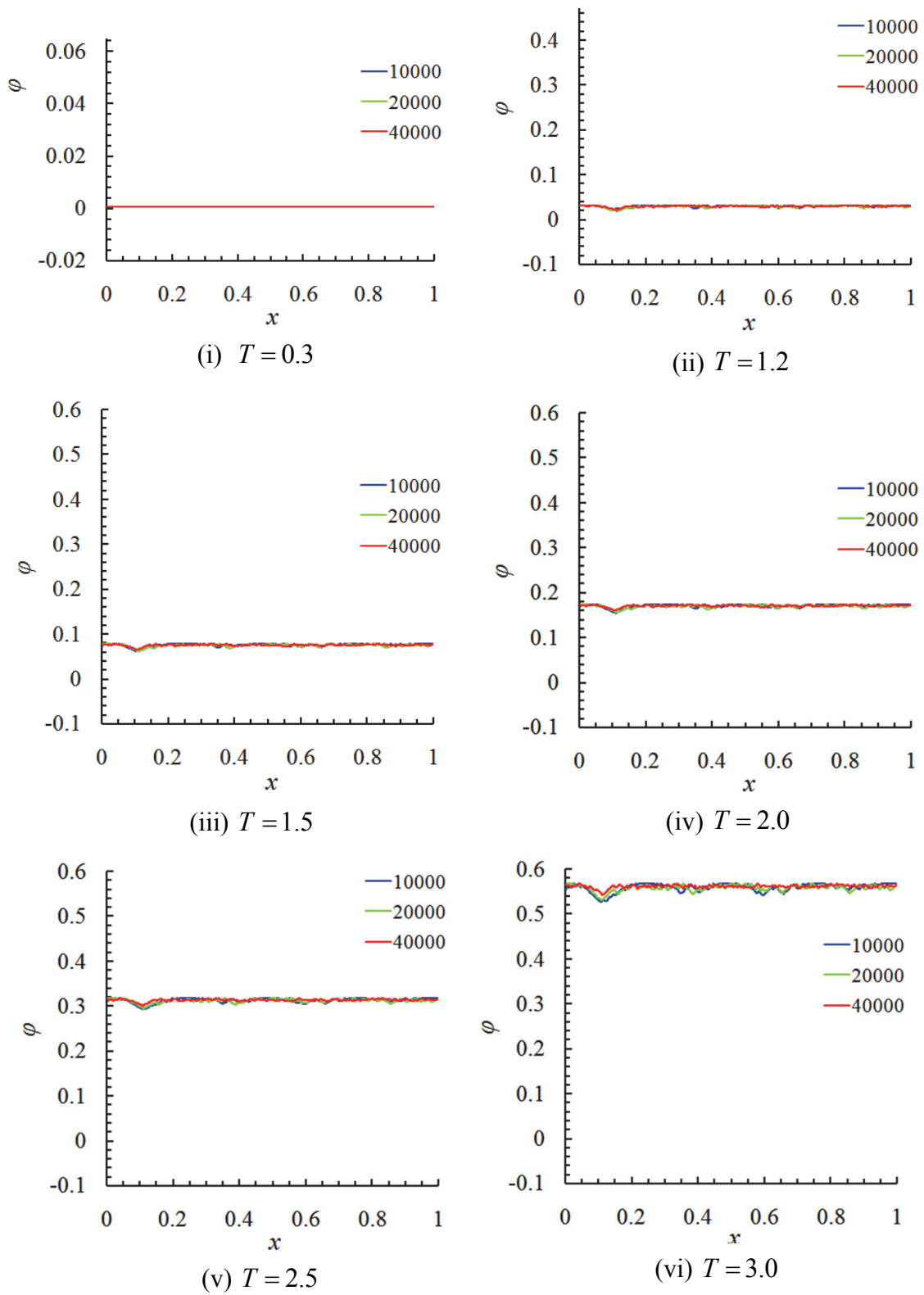
(v) $T = 2.5$

(vi) $T = 3.0$

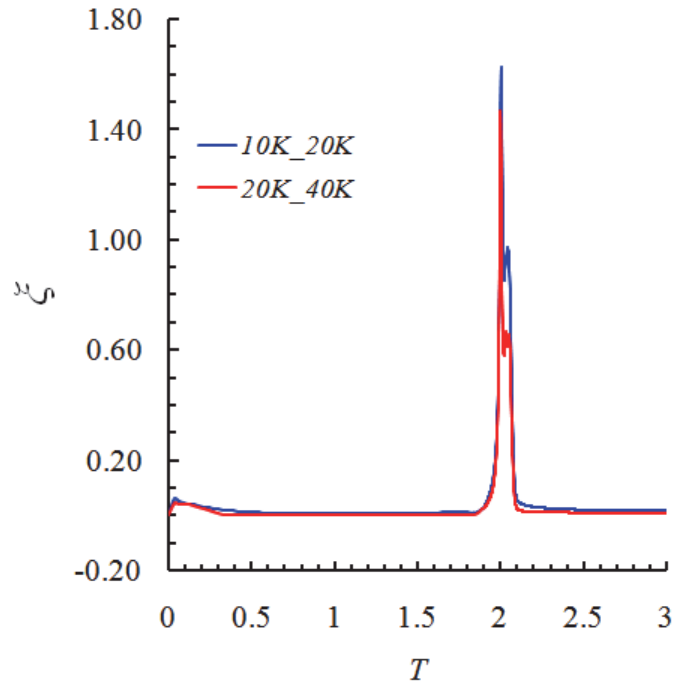Fig. 9 (c) Convergence of φ evolution for Case IV

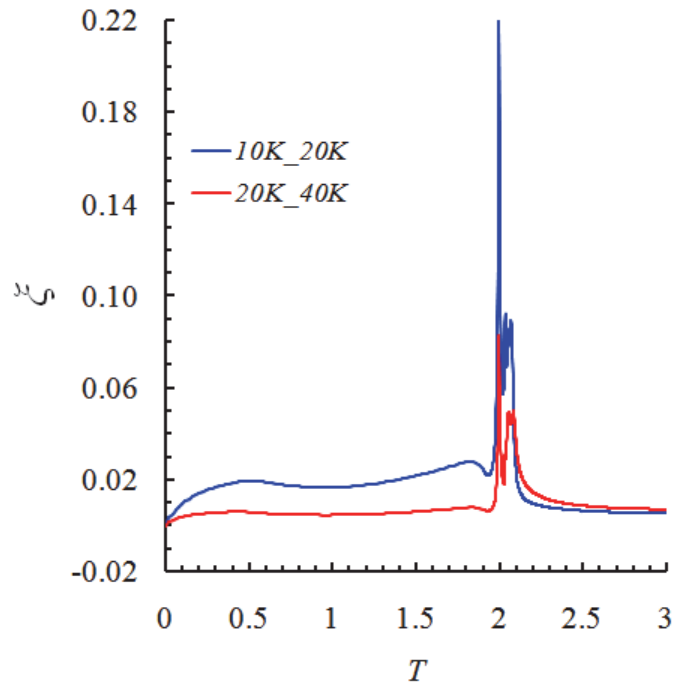Fig. 10 (a) Variation of error for Case I

Fig. 10 (b) Variation of error for Case I with high value of ε^* and low N
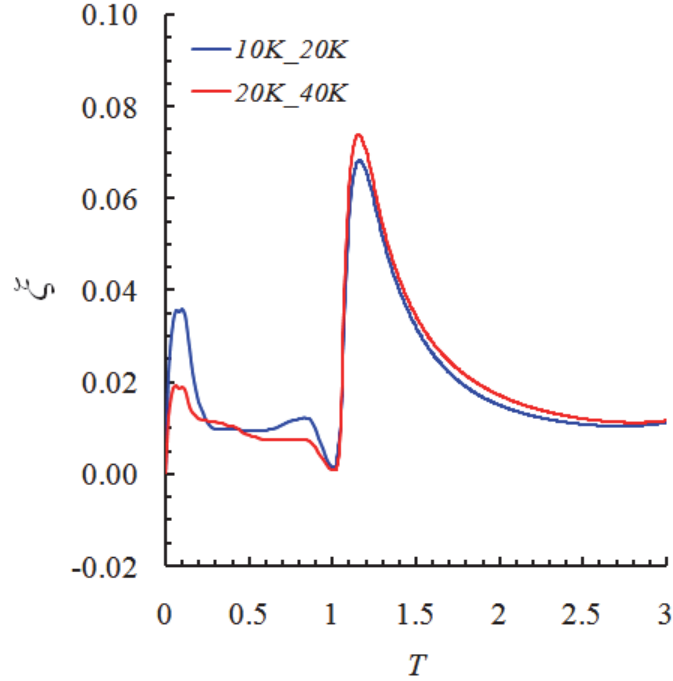
Fig. 10 (c) Variation of error for Case IV

4. Conclusions

This paper demonstrates that

- Transport of polar dislocation density coupled with gradient hardening with *no non-monotone equations of state* can give rise to spatial patterning in a mechanically rigorous model of mesoscale continuum plasticity and dislocation mechanics.
- Non-monotone equations of state of a certain type induce stick-slip behavior.
- The presence of transport of polar dislocation density appears to be essential for the prediction of spatial patterning.
- Development of neither large-scale inhomogeneity nor stick slip behavior is predicted by the conventional plasticity model.
- Convergence is achieved for a low wave number initial condition and incorporation of an effective mesoscale core energy in the model. Convergence can be achieved for a high wave number initial condition in the absence of non-monotone equations of state.
- In the limit as the regularization due to the core energy vanishes (or the macroscopic limit), the model with non-monotone equation of state shows oscillations and sensitivity to the mesh resolution and to the initial data which are typical of weak convergence of the solutions. The limit problem and the type of convergence for the solutions remain to be studied but cannot be obtained by simply setting $\varepsilon = 0$ in the equations. By contrast, in the absence of non-monotone equation of state, convergence is achieved even for a high wave-number initial condition.

41

Acknowledgment

References

Abeyaratne, R., Chu, C., & James, R. D. (1996). Kinetics of materials with wiggly energies: theory and application to the evolution of twinning microstructures in a Cu-Al-Ni shape memory alloy. *Philosophical Magazine A*, *73*(2), 457-497.

Acharya, A. (2010). New inroads in an old subject: plasticity, from around the atomic to the macroscopic scale. *Journal of the Mechanics and Physics of Solids*, *58*(5), 766-778.

Acharya, A., & Beaudoin, A. J. (2000). Grain-size effect in viscoplastic polycrystals at moderate strains. *Journal of the Mechanics and Physics of Solids*, *48*(10), 2213-2230.

Acharya, A., & Roy, A. (2006). Size effects and idealized dislocation microstructure at small scales: predictions of a phenomenological model of mesoscopic field dislocation mechanics: Part i. *Journal of the Mechanics and Physics of Solids*, *54*(8), 1687-1710.

Acharya, A., Tang, H., Saigal, S., & Bassani, J. L. (2004). On boundary conditions and plastic strain-gradient discontinuity in lower-order gradient plasticity. *Journal of the Mechanics and Physics of Solids*, *52*(8), 1793-1826.

Acharya, A., & Tartar, L. (2011). On an equation from the theory of field dislocation mechanics. *Bollettino dell'Unione Matematica Italiana*, *9*, 409-444.

Aifantis, E. C. (1984). On the microstructural origin of certain inelastic models. *Journal of Engineering Materials and technology*, *106*(4), 326-330.

Barenblatt, G. I. (1996). *Scaling, self-similarity, and intermediate asymptotics: dimensional analysis and intermediate asymptotics* (Vol. 14). Cambridge University Press.

Chen, Y. S., Choi, W., Papanikolaou, S., & Sethna, J. P. (2010). Bending crystals: Emergence of fractal dislocation structures. *Physical Review Letters*, *105*(10), 105501.

Chen, Y. S., Choi, W., Papanikolaou, S., Bierbaum, M., & Sethna, J. P. (2013). Scaling theory of continuum dislocation dynamics in three dimensions: Self-organized fractal pattern formation. *International Journal of Plasticity*, *46*, 94-129.

Choi, W., Chen, Y. S., Papanikolaou, S., & Sethna, J. P. (2012). Is dislocation flow turbulent in deformed crystals?. *Computing in Science & Engineering*, *14*(1), 33-39.

Das, A., Acharya, A., Zimmer, J., & Matthies, K. (2013). Can equations of equilibrium predict all physical equilibria? A case study from Field Dislocation Mechanics. *Mathematics and Mechanics of Solids*, *18*(8), 803-822.

Dimiduk, D. M., Woodward, C., LeSar, R., & Uchic, M. D. (2006). Scale-free intermittent flow in crystal plasticity. *Science*, *312*(5777), 1188-1190.

Glazov, M., Llanes, L. M., & Laird, C. (1995). Self-organized dislocation structures (SODS) in fatigued metals. *physica status solidi (a)*, *149*(1), 297-321.

Kreiss, H. O., & Lorenz, J. (1989). *Initial-boundary value problems and the Navier-Stokes equations*, Vol. 47 of Classics in Applied Mathematics Series, SIAM.

Kurganov, A., Noelle, S., & Petrova, G. (2001). Semidiscrete central-upwind schemes for hyperbolic conservation laws and Hamilton--Jacobi equations. *SIAM Journal on Scientific Computing*, *23*(3), 707-740.

Limkumnerd, S., & Sethna, J. P. (2006). Mesoscale theory of grains and cells: crystal plasticity and coarsening. *Physical Review Letters*, *96*(9), 095503.

Mughrabi, H., Ackermann, F. U., & Herz, K. (1979). Persistent slip bands in fatigued face-centered and body-centered cubic metals. *Fatigue Mechanisms, ASTM STP*, *675*, 69-105.

Ortiz, M., & Repetto, E. A. (1999). Nonconvex energy minimization and dislocation structures in ductile single crystals. *Journal of the Mechanics and Physics of Solids*, *47*(2), 397-462.

Parthasarathy, T. A., Rao, S. I., Dimiduk, D. M., Uchic, M. D., & Trinkle, D. R. (2007). Contribution to size effect of yield strength from the stochastics of dislocation source lengths in finite samples. *Scripta Materialia*, *56*(4), 313-316.

Rice, J. R. (1971). Inelastic constitutive relations for solids: an internal-variable theory and its application to metal plasticity. *Journal of the Mechanics and Physics of Solids*, *19*(6), 433-455.

Roy, A., & Acharya, A. (2006). Size effects and idealized dislocation microstructure at small scales: predictions of a phenomenological model of mesoscopic field dislocation mechanics: Part II. *Journal of the Mechanics and Physics of Solids*, *54*(8), 1711-1743.

Tartar, L. (2009) The General Theory of Homogenization. *Lecture Notes of the Unione Matematica Italiana*, *7*, Springer, Heidelberg.

Xia, S., & El-Azab, A. (2015). Computational modelling of mesoscale dislocation patterning and plastic deformation of single crystals. *Modelling and Simulation in Materials Science and Engineering*, *23*(5), 055009.

Walgraef, D., & Aifantis, E. C. (1985). On the formation and stability of dislocation patterns—I: One-dimensional considerations. *International Journal of Engineering Science*, *23*(12), 1351-1358.

Walgraef, D., & Aifantis, E. C. (1985). On the formation and stability of dislocation patterns—II: Two-dimensional considerations. *International Journal of Engineering Science*, *23*(12), 1359-1364.

Walgraef, D., & Aifantis, E. C. (1985). On the formation and stability of dislocation patterns—III: Three-dimensional considerations. *International Journal of Engineering Science*, *23*(12), 1365-1372.

Zhang, X., Acharya, A., Walkington, N. J., & Bielak, J. (2015). A single theory for some quasi-static, supersonic, atomic, and tectonic scale applications of dislocations. *Journal of the Mechanics and Physics of Solids,* 84, 145-195.

Appendix1

Simplified one-dimensional form of conservation law of Burgers vector content

The conservation law for Burgers vector content in mesoscale field dislocation mechanics is given by

$$\dot{\boldsymbol{\alpha}} = -curl\left(\boldsymbol{\alpha} \times \boldsymbol{V} + \boldsymbol{L}^p\right) \tag{A1.1}$$

where $\boldsymbol{\alpha}$ is the mesoscale Nye tensor, $\boldsymbol{V}$ is the mesoscale averaged dislocation velocity vector, and $\boldsymbol{L}^p$ is the plastic strain rate produced by unresolved, at the mesoscale, and hence 'statistical' dislocations (Acharya and Roy, 2006). Here,

$$-curl\,\boldsymbol{U}^p = \boldsymbol{\alpha}\,. \tag{A1.2}$$

Consider a tensor field of the form

$$\boldsymbol{A} = A_{12}\boldsymbol{e}_1 \otimes \boldsymbol{e}_2 \tag{A1.3}$$

and we assume that all fields vary in only the x_3 direction. Then the only non-zero component of

$$\left(curl\,\boldsymbol{A}\right)_{ri} = e_{ijk} A_{rk,j} \tag{A1.4}$$

is

$$\left(curlA\right)_{11} = e_{132} A_{12,3} = -A_{12,3}\,. \tag{A1.5}$$

We assume the ansatz

$$\begin{aligned}
\boldsymbol{U}^p &= U^p_{12}\,\boldsymbol{e}_1 \otimes \boldsymbol{e}_2 \\
\boldsymbol{L}^p &= L^p_{12}\,\boldsymbol{e}_1 \otimes \boldsymbol{e}_2 \\
\boldsymbol{\alpha} &= \alpha_{11}\,\boldsymbol{e}_1 \otimes \boldsymbol{e}_1 \\
\boldsymbol{V} &= V_3\,\boldsymbol{e}_3.
\end{aligned} \tag{A1.6}$$

Then

$$\boldsymbol{\alpha} \times \boldsymbol{V} = -\alpha_{11} V_3\,\boldsymbol{e}_1 \otimes \boldsymbol{e}_2 \tag{A1.7}$$

$$-\left[curl\left(\boldsymbol{\alpha} \times \boldsymbol{V}\right)\right] = -\left[-\left(-\alpha_{11} V_3\right)_{,3}\right]\boldsymbol{e}_1 \otimes \boldsymbol{e}_1 \tag{A1.8}$$

$$-curl\,\boldsymbol{L}^p = -\left[-L^p_{12,3}\right]\boldsymbol{e}_1 \otimes \boldsymbol{e}_1 \tag{A1.9}$$

$$\boldsymbol{\alpha} = -curl\,\boldsymbol{U}^p = -\left[-U^p_{12,3}\right]\boldsymbol{e}_1 \otimes \boldsymbol{e}_1\,. \tag{A1.10}$$

Denoting $U^p_{12} = \varphi$, $x_3 = x$, $x_1 = y$, $x_2 = z$, $V_3 = V$, and $L^p_{12} = L^p$ the conservation law reduces to the equation

$$\left(\varphi_x\right)_t = -\left(\varphi_x V - L^p\right)_x\,. \tag{A1.11}$$